REPRODUCIBILITY AND USE OF MYELIN IMAGING METHODS FOR THE STUDY OF ADOLESCENT BRAIN DEVELOPMENT

A Dissertation
submitted to the Faculty of the
Graduate School of Arts and Sciences
of Georgetown University
in partial fulfillment of the requirements for the
degree of
Doctor of Philosophy
In Neuroscience

By

Erika P. Raven, B.S.

Washington, DC
July 13, 2017

REPRODUCIBILITY AND USE OF MYELIN IMAGING METHODS FOR THE STUDY OF ADOLESCENT BRAIN DEVELOPMENT

Erika P. Raven, B.S.

Thesis Advisors: John VanMeter, Ph.D. and Jeff Duyn, Ph.D.

ABSTRACT

Human brains have few myelinated axons at birth and continue to myelinate along a temporal and regional specific pattern into adulthood. This prolonged growth trajectory not only contributes to adaptability in functional circuitry, but also presents a vulnerability to certain psychiatric and behavioral disorders. MRI is highly sensitive to tissue constituents such as myelin membranes, but standard imaging techniques are typically limited to depicting macrostructure, such as gross white matter volumes and fiber tracts. More recently, quantitative *in vivo* myelin imaging has improved via developments in tissue modeling, pulse sequence design, and use of ultra high-field scanners. This dissertation examines the reproducibility and application of two recently developed MRI techniques with sensitivity to myelin content in white matter. First, multi-exponential modeling of multiple gradient echo T_2* decay curves was used to extract an estimate of myelin content, i.e., myelin water fraction (f_{MW}), at two field strengths (3 T and 7 T) using *in vivo* and simulated data. At 3 T, model parameters were dominated by noise when compared to 7 T; however, artifacts impeded the assessment of *in vivo* results at 7 T for use in future studies. To further generalize the effects of noise and myelin parameter estimation, the T_2*-based myelin water estimate, f_{MW}, was compared to an alternative indicator of myelin content, the macromolecular proton fraction (f_{MT}), using a newly developed magnetization transfer (MT) technique. All data were acquired at 3 T in

a cohort of healthy adolescents (ages 12.7 – 16.8). The f_{MT} was ten times less variable, and thus more reproducible, versus the f_{MW}. For the final study, the MT approach was applied in a longitudinal study of healthy adolescent development. Here, f_{MT} was found to significantly increase in frontal white matter ($p=0.003$) over an 18 month delta in mid- to late-adolescence. There were no changes greater than 15% for any white matter region; in addition, changes within individuals were relatively small, averaging 2.5% for the frontal region. As myelin imaging techniques are becoming more widely used, these studies are important for understanding the sensitivity and reproducibility of new measures prior to widespread use in clinical and research applications.

ACKNOWLEDGEMENTS

I'd like to share my immense thanks to an unbelievable group of family, friends, and colleagues. First, thank you to my thesis co-advisors, John VanMeter and Jeff Duyn for granting me the flexibility to explore new ideas along an often circuitous path. I have truly valued your guidance, perspective, and thoughtful mentorship.

To my lab advisor, Peter van Gelderen - thank you for challenging me and being unendingly patient. I am grateful to have learned so much from you.

With two thesis labs, comes the benefit of twice the labmates. To CFMI/ADS – thank you for supporting my projects, even when said projects (temporarily) disrupted the scanner. To AMRI - the quadrant has been my home base, and that goes without saying how special everyone in the lab and the surrounding halls of NIH have made this experience. In particular, thank you Catie Chang for listening, teaching, and always smiling.

To those far and wide - thank you Dominic Hare and Nikola Stikov for your mentorship and fostering my enthusiasm for collaboration.

To those close to home - thank you for making DC the best possible place to study and grow as a scientist. Britt, Caitlin, Lauren, Patrick, and Brian - thank you for your constant support and happiness, at any and all times. To those at home - thank you Teddy, Steph, and Mariam for making Salem Lane such a magical place.

Thank you family. I have relied on your love and support with every phone call, text, picture, handwritten card, and email. I'd also like to send a very special thanks to my mom, Marit, for illustrating the figures in Chapter 1.

To my husband Danny – thank you for your unwavering love and encouragement, and for convincing me/us it was a good idea to leave California on this adventure. This is for you.

And finally, I am honored to share the memory of George Bartzokis (August 19, 1956 – August 22, 2014) and Karen Gale (October 14, 1948 – August 21, 2014), who unequivocally inspired this wild ride.

"There is a grandeur in this view of life, with its several powers, having been originally breathed into a few forms or into one; and that, whilst this planet has gone cycling on according to the fixed law of gravity, from so simple a beginning endless forms most beautiful and most wonderful have been, and are being, evolved." - Charles Darwin

TABLE OF CONTENTS

LIST OF FIGURES

LIST OF TABLES

LIST OF ABBREVIATIONS AND SYMBOLS

A_n	Amplitude of water component
AC–PC	Anterior commissure – posterior commissure
B_0	Static magnetic field
CNS	Central nervous system
EPI	Echo-planar imaging
mcDESPOT	Multi-component driven equilibrium single pulse observation of $T_{1,2}$
FLWM	Frontal lobe white matter
EF	Executive function
f_{MT}	Macromolecular proton fraction
f_{MW}	Myelin water fraction
f_n	Frequency shift relative to the global frequency
f_g	Global frequency, used for interstitial water pools
GCC	Genu of corpus callosum
i	Imaginary unit
MGRE	Multiple gradient echo
MP	Macromolecular protons
MRI	Magnetic resonance imaging
MSE	Multiple spin echo
MT	Magnetization transfer
MW	Myelin water
MWF	Myelin water fraction, standard notation
NNLS	Non-negative least squares
OR	Optic radiation
R_2*	Net transverse relaxation rate, $1/T_2$*
ROI	Region of interest
SCC	Splenium of corpus callosum
SNR	Signal-to-noise ratio
SWM	Spatial working memory
T	tesla (SI unit of magnetic flux density)
T_1	Longitudinal relaxation time
T_2	Irreversible transverse relaxation time
T_2’	Reversible transverse relaxation time
T_2*	Net transverse relaxation time
TE	Echo time
TR	Repetition time
TMT-B	Trail making test, part B
WP	Water protons
φ	Phase offset

Chapter I. Introduction

The organization of the central nervous system (CNS), including the brain and spinal cord, has classically been divided into white and gray matter. In humans, around 40 percent of the brain contains white matter, which is a lighter color due to its exceptionally high lipid content. At a cellular level, white matter is comprised of densely packed, cylindrical projections, i.e., axons of neurons, that are frequently surrounded by thin, fatty membranes called myelin sheaths. Famed pathologist Louis-Antoine Ranvier, influenced by events of the late 1860s, equated these ensheathed projections to the first undersea telegraph cables [1]. Similar to cables, bundles of white matter fibers transmit information to and from various targets, such as cortical gray matter and subcortical nuclei. Gray matter is densely populated by neuronal cell bodies and their dendritic projections, which receive and integrate signals from adjoining neurons. The complex, interconnected networks of neurons form the basis of sensation, perception, and behavior in the brain. There are approximately 85 billion of these cells in the adult brain, with an estimated 100 trillion synaptic connections between them [2,3]. While these numbers are extraordinary, there are nearly equal numbers of non-neuronal cell types, called glia [4]. Glia, meaning Greek for "glue," were once believed to be the connective tissue holding neurons in place [5]. With the advent of better and more powerful imaging technologies, the morphology of glia have been expanded to include oligodendrocytes, astrocytes, microglia, and progenitor cells. These cells perform a variety of essential tasks, and disruption in their number or function has been shown to result in many neurologic and psychiatric diseases [6]. Of the four non-neuronal cells, oligodendrocytes are the most abundant glial cell type in white matter. Oligodendrocytes

produce the fatty membrane extensions that wrap tightly around the axonal brain "cables." While speculating on the purpose of myelin, Ranvier wrote this in 1878:

> "I do not think, I wish you to note, that this insulating myelin sheath is necessary for the transmission of impulses … I think that this insulation serves to make it more perfect." (Ranvier, 1878) [1]

While this statement is still true today, we now know the role of myelin goes far beyond that of an electrical insulator. This chapter will discuss the primary function and structure of myelin, and present evidence of its adaptability throughout development. The final section will discuss magnetic resonance imaging (MRI) techniques used to characterize white matter, with a focus on methods for estimating the relative myelin content in tissue.

1.1 Myelin in the central nervous system

1.1.1 Signal conduction

Myelin is pervasive throughout white matter, and to a lesser degree gray matter regions like the cortex, which is due to its essential role in neuronal signal conduction. To better understand this advantage, we first discuss the basic properties needed to send a signal. At rest, neurons must tightly regulate the distribution of sodium and potassium ions on either side of the surface of the neuron. This creates a difference in voltage across the membrane, with the inside surface being more negative. When a sufficiently large voltage change, or depolarization, occurs, the neighboring areas of membrane are also depolarized. This effect is propagated as specialized channels are opened, and ions are allowed to flow to the opposite side of the membrane from their existing location, or down their electrochemical gradient. This temporary flow of ions

creates a continuous wave of electrical current called the action potential. The action potential triggers the release of neurotransmitters for signaling adjoining neurons or various target tissues in the body. In an unmyelinated axon, the velocity of signal conduction is related to the length and diameter of its axon. Invertebrates do not have myelin, and have compensated for increases in body size, thus, longer axons, by increasing axonal diameter. This is spectacularly demonstrated in the Atlantic squid, which is approximately 0.3 meters in length, but has a giant axon of 0.5 to 1 mm in diameter [7,8]. The squid giant axon is approximately 15,000 times larger than what is needed for a comparable myelinated mammalian axon and requires several thousand times more energy to maintain [9]. To translate into human dimensions, the spinal cord would need to be nearly 1 meter in diameter to maintain current functionality without myelin. This is clearly not possible for vertebrates, as there are limitations due to available space within the skull and vertebral column, as well as the high-energy demands of complex circuitry in the CNS.

Myelin sheaths allow for fast and efficient action potentials via the process of saltatory conduction. When a neuron fires an action potential, the depolarization process skips over myelinated segments to only depolarize at small, exposed gaps, called the nodes of Ranvier. These gaps occur sequentially, and at widely separated intervals in the sheath. Myelin has an exceptionally high lipid content (~70%) and acts as an electrical insulator. As such, it prevents the leakage of current from within the axon (increases resistivity) and reduces the membrane's ability to store charge (lowers capacitance). Depolarization is then restricted to finite regions, and current can travel super fast from node to node versus leaking back across the membrane. Myelin can additionally modulate the conduction velocity by changing the thickness of the myelin sheath, the number and spacing of nodes of Ranvier, and nodal structure and molecular composition of ion channels in the node itself (reviewed in [10]).

Figure 1.1 Cross-section of a myelinated peripheral axon. The myelin sheath is formed by thin layers of membrane wrapped tightly around the neuronal axon (~1 μm across). For axons with diameters larger than 0.2 μm, myelin thickness is roughly proportional to the diameter of the axon.

In the human brain, axon diameters can range from 0.1 up to 10 μm in central white matter [11–13]. Previous studies have demonstrated that the thickness of myelin sheath is proportional to axonal diameter, with larger axons having thicker myelin sheaths (and vice versa for smaller axons) [14–16]. This was first reported by Schmitt and Bear (1937) using light refraction (birefringence) in myelinated axons of different total diameters [17]. The ratio of axonal diameter (inner) to total fiber diameter (outer), i.e., the g-ratio, was so named from their gamma measurement of refraction. They also observed that axons of less than 2 μm in diameter were typically unmyelinated. In 1951, Rushton proposed a theoretical g-ratio of 0.6 for optimal conduction velocity of peripheral nerve fibers, and showed that small diameter fibers (<1 μm) did not benefit from the increased resistivity of myelin [18]. In CNS, the average g-ratio has been estimated to be ~0.77 (i.e., thinner myelin sheaths), possibly reflecting the different space, energy, and timing requirements of these tissues [14]. Variations have been reported experimentally

for g-ratios between different brain regions, fiber bundles, and even individual axonal projections [11,19,20]. There are also unmyelinated axons of varied diameters throughout the CNS. For example, the corpus callosum, i.e., the largest, interhemispheric white matter tract in the brain, was found to have up to 16% unmyelinated axons ranging in diameter of 0.1 to 1.0 μm [11]. The heterogeneity of callosal axon diameters and myelin content result in widely varied conduction times of 150-300 ms (unmyelinated) to 30 ms (myelinated) between left and right hemispheres of the brain [10]. The diversity of myelinated axons indicates that achieving the fastest speed possible is not the only objective of neuronal communication. By modulating the myelin content of these circuits, neuronal signals can be "tuned" to dynamically speed up or delay either excitatory or inhibitory inputs as they converge on postsynaptic targets [10,20]. Fine control of neuronal timing is especially important, as large populations of neurons must coordinate their responses for optimizing the cognitive and behavioral function of particular networks [21].

1.1.2 Myelin sheath formation

The formation of myelin sheaths is associated with the synthesis of vast amounts of membrane by oligodendrocytes. The glial origin of myelin was not always apparent, and took the development of the electron microscope to debunk a long-standing controversy that axons secreted myelin in response to cellular activity. In 1954, Betty B. Geren was the first to show definitive proof that glial cells were indeed responsible for myelination of peripheral nerves [22]. She published electron micrographs at different stages of embryonic myelin formation, which also highlighted the spectacular spiral wrapping mechanism around stationary axons. Almost ten years later, Mary Bunge and colleagues were able to show a similar process for oligodendrocytes in much smaller axons of the CNS [23].

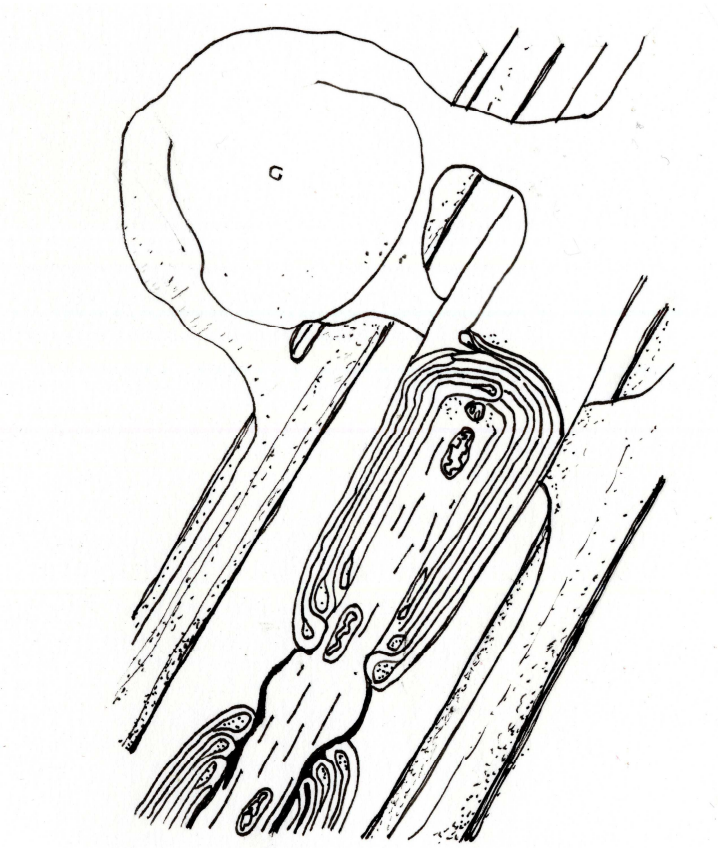

Figure 1.2 Oligodendrocyte sending projections to several axons. Myelin membranes have been cut away (foreground), exposing the multi-layered myelin sheath and longitudinal section of a single axon. The axonal swelling is the node of Ranvier. Figure adapted from [24].

The formation of myelin, aptly described by the "jelly-roll" model, involves the coordinated extension of the oligodendrocyte cell membrane as it inwardly wraps around an axon. Additional wraps are obtained by lengthening the membrane from the inner tongue (adjacent to the axon), where it is continuously moving beneath the previously formed layers [25]. Recent work has shown that CNS myelin also extends laterally during this process, to control the length of each myelin segment [26]. Myelin segments, or internodes, can be as long as 1 mm and separated by gaps of 1 μm [15]. A final step of myelination is membrane compaction, which binds the inner face of each membrane layer to squeeze out axonal cytoplasm. This forms the alternating, dark dense lines seen on electron microscopes in mature myelin sheaths. The number of myelin wraps and total

membrane internodes can vary widely between oligodendrocytes. The length of internodes is also variable, as is the number of axons a single oligodendrocyte can myelinate. These characteristics are dependent on many factors, including the diameter of axons and the region of the CNS that is being myelinated. This is in addition to changes in myelin with age and neuronal activity (discussed in the next section). In summary, oligodendrocytes form a heterogeneous and modifiable pattern of myelination throughout the brain, and new research continues to uncover the dynamics of these effects.

The molecular composition of myelin is ~70% lipids (dry weight), including galactosphingolipids, certain phospholipids, saturated long-chain fatty acids, and cholesterol [27,28]. The lipids are assembled into bilayers, meaning two lipid layers form the surface of the myelin membrane. Bilayers are a common feature of cellular membranes and create a semi-permeable boundary for the watery inner and outer environments of a cell. Each composite molecule assembles into the bilayer with their hydrophilic (water-loving) polar heads facing outward, and their hydrophobic (water-fearing) tails facing inward [29]. If myelin wraps were to be completely unrolled from one segment, there would be two sets of bilayers (four layers of lipids total) comprising the entirety of the flattened membrane. The outermost lipids would be exposed to the extracellular matrix, and the innermost lipids would be adjacent to the cytosol of the oligodendrocyte. Myelin membranes are highly organized, due to the stratification of each wrap, and the radial orientation of lipid molecules relative to the cylinder-like axon. The periodic array of multiple layers is unique to myelin, as is the low fraction of proteins (~30% of dry weight) used for cytosolic compaction and the stability of myelin structure. The aqueous spaces between the hydrophobic bilayers of myelin wraps comprise about one-third of myelin thickness [30]. These

spaces include mostly water and some proteins; as such, water is estimated to be ~40% of the total myelin volume (e.g., lipids, proteins, water) [30].

1.1.3 Myelin development and plasticity

Myelin development follows a prescribed sequence, with distinct fiber tracts being myelinated at specific times [31,32]. In general, pathways of sensory systems mature before motor, and projection before association. Paul Flechsig (1920) proposed that serial myelination was dependent on the requirements of a system, which mirrored the increasing complexity of brain functions throughout development [31]. In humans, the onset of CNS myelination begins in utero at 16 weeks of gestational age [32]. Regions for basic homeostatic, motor, and sensory processing mature within the first year, while regions involved in higher order tasks, such as the frontal and temporal cortex, continue to actively myelinate into adulthood. The post-pubertal growth of myelin is unique to humans [33], and not coincidentally the development of later-myelinating regions coincides with improvements in executive and social cognitive functions during adolescence and adulthood [34]. After "peak" maturity is reached, there is a period of stability and subsequent decline into older age, resembling an inverted U-shaped trajectory across the lifespan [35,36]. Brain regions that are relatively slow to mature throughout adolescence, also happen to have accelerated degeneration into older age [37]. This pattern, called the "last-in, first-out" or retro-genesis model of development, describes association cortices and neostriatum (i.e., phylogenetically young brain areas) as being vulnerable to damage due to processes associated with aging and disease [37]. These regions were last to evolve and have more complex structural elements, such as oligodendrocytes that form a large number of internodes and fewer myelin wraps. The characteristics of late-forming myelin are more adaptable for fine-tuning the

multimodal integration of association cortices, however, they are less robust to oxidative stressors and negative environmental factors. As such, last-in regions are preferentially vulnerable to myelin dysfunction [38].

Myelination is not strictly a developmental program, and can be modified based on new experiences and various environmental factors. Animal studies have shown both increases in myelinated axons and volume of corpus callosum when being exposed to enriched environments [39]. Conversely, negative stimuli, such as nutritional deficits or social isolation, have shown hypomyelination in both animals and humans [40]. These effects appear to be especially sensitive to critical periods in very early development (around the third trimester to first two years for humans), resulting in permanent functional deficits throughout the lifespan [41,42]. Even so, the adult brain contains a large, and highly mobile supply of oligodendrocyte progenitor cells (OPCs). OPCs can differentiate into mature oligodendrocytes to effectively generate new myelin. These cells are a remarkable source of plasticity, and are also used to repair existing myelin sheaths. In a study of adult mice, the formation of new oligodendrocytes, and thus new myelin, was necessary for learning a complex motor task [43]. Interestingly, the adult-born oligodendrocytes produced more frequent, but shorter segments of myelin in response to the stimuli. These experiments highlight the adaptability of this process, and that the formation of new myelin is closely linked to neuronal activity. Human studies using *in vivo* magnetic resonance imaging (MRI) have also found differences in white matter structure after learning a complex task, such as juggling or playing the piano [44]. While MRI is generally considered nonspecific to cellular-level changes, these examples coincide with the idea that new myelin is formed preferentially on circuits being activated during learning.

1.2 Noninvasive imaging of the brain

MRI uses strong magnetic fields and radiofrequency signals to manipulate hydrogen nuclei (i.e., protons) within the abundant water reservoirs of biological tissues. When a person is placed inside the magnetic field of a scanner, a very tiny percentage of hydrogen protons align along the direction of the external field (B_0). Radiofrequency waves are applied in short bursts, or pulses, at the resonance frequency of hydrogen to specifically excite the aligned protons; after which, they re-emit signals also in the form of radiofrequency waves. MRI resonance frequencies are proportional to the strength of the magnetic field. As such, magnetic field gradients (in addition to B_0) are used to introduce subtle variations in field strength across the imaging slice, thus allowing for the localization (via changes in frequencies) of hydrogen protons. Based on the nature of these signals, we can then infer the local magnetic environment and densities of the many trillions of hydrogen protons within an imaging plane. These signals are ultimately transformed into the varied contrasts seen in an MR image.

The spatial resolution of an MR image (i.e., voxel size) is typically ~ 1 mm^3 for clinical scanners, which is roughly three orders of magnitude greater than the cellular structures within a voxel. For example, one cubic millimeter of cortical gray matter is densely packed with neuronal cell bodies and dendritic processes, as well as 10,000 to 60,000 axons, blood vessels, intra-cortical myelin, and glial cells [45–47]. Improving image resolution (i.e., smaller voxels) is of great interest to better resolve tissue types. Ultra-high field scanners (7 T and above) have achieved ~250 μm in-plane resolution in living human brain; however, decreasing voxel size requires a tradeoff of technical and practical constraints and is still unable to achieve the resolution of cellular features, such as myelin thickness and axonal structure [48]. In any event, MRI allows for

the visualization of brain macrostructure in exquisite detail, which has led to its widespread use for studying white matter in the brain.

1.2.1 Techniques for studying white matter and myelin in vivo

MRI methods have been developed to study different characteristics of white matter. The hydrogen protons of myelin proteins and lipids do not contribute to the observed MRI signal, but may affect it indirectly. This section will briefly discuss the basic contrast mechanisms of MRI, and how we can use this information to visualize and infer changes in white matter structure.

> "MRI is magnetic interrogation of tissues: We ask a question of the tissues, listen to the body's answer, and analyze the response." (William Oldendorf, 1991) [49]

The "question" in MRI is asked by the design of the radiofrequency (RF) pulses, gradient changes in the static magnetic field, and acquisition parameters of the imaging sequence. Sequences can be quite complex, e.g., using different pulse types and amplitudes, repetition times, echo times, etc.; while attempting to elicit specific information from tissues. After the RF pulse sequence is applied, hydrogen protons begin to lose energy as they relax back to their pre-stimulated state. This process is described by changes in net magnetization, or the vector sum of all signals from the hydrogen protons. The magnetization can be analyzed in terms of two component vectors. First, the longitudinal component reflects the loss of energy due to the realignment of protons with B_0. Independent from energy losses, protons are locked in phase immediately after the pulse, and oscillate (precess) at the same frequency. Second, in-phase precession does not last for long due to the molecular interactions. As such, the transverse

component measures the rate of de-phasing of hydrogen protons. Depending on tissue composition within a voxel, the protons will experience different rates of longitudinal and transverse relaxation as described by their time constants - T_1 and T_2. In addition, T_2 dephasing can be accelerated by non-uniformities in the magnetic field (T_2'). The combined effects of T_2 and magnetic field distortions (T_2') are called T_2*. There are other mechanisms that contribute to image contrast, such as magnetization transfer, chemical shift, diffusion, and others. The complex interaction of these mechanisms is the "body's answer" to its magnetic environment. To interpret the "response," we have to go back to the question. That is, depending on what kind of method (pulse sequence, gradients, and acquisition parameters) is used to excite the tissues, will result in a specific kind of signal behavior, and thus direct what kind of analysis should be performed.

T_1-weighted imaging and diffusion weighted imaging are common techniques used to study white matter. T_1-weighted images have excellent soft tissue contrast, as they are "weighted" for the best visual presentation of different tissue types. The analysis of these images typically includes segmentation of gray and white matter structures to assess average lobar or cortical volumes. This technique can provide a macroscopic view of white matter changes, and has been used extensively in longitudinal studies. However, this contrast is sensitive to a combination of effects, including myelin content and cellular density [50], as well as changes in relaxivity due to variations in water content and scanner parameters [51]. Conversely, diffusion weighted imaging measures the net displacement of water protons over a set period of time. If the diffusion time is sufficiently long, the random motion of water will be hindered by the surrounding microstructure of tissue. This is especially apparent in white matter, as myelinated axons are organized into long fiber bundles. Diffusion weighted images can be modeled as a

tensor, and various metrics, such as fractional anisotropy and mean diffusivity, are then calculated to describe the directionality of this behavior [52]. The diffusion metrics are also sensitive to many biological factors, such as myelination, density and number of axons, membrane permeability, and intra-voxel dispersion of fibers [53]. A pervasive issue with both of these techniques is that a range of cellular features can lead to similar changes in signal intensity. For this reason, alternative imaging techniques are being investigated for imaging myelin in human brain. Two such techniques were chosen for use in this thesis, myelin water and magnetization transfer imaging, and are described below.

1.2.2 Myelin water imaging

Standard imaging techniques assume water is well mixed within each voxel, and can be represented by a single T_1 or T_2 value. This is not the case in white matter, as water is temporarily restricted to distinct cellular environments by multi-layered myelin membranes. Vasilescu et al (1978) demonstrated the presence of three experimentally distinct T_2 relaxation components in myelinated frog nerve [54]. Using nuclear magnetic resonance (NMR), T_2 values were acquired at multiple time points (echo times) to produce the full evolution of T_2 signal decay. Transverse relaxation resembles an exponential decay function as increases in dephasing contribute to signal loss over time. The Vasilescu study fit a multi-exponential function to the T_2 signal, and found fast, intermediate, and slowly relaxing components. The authors suggested these rates were from water associated with proteins and phospholipids, axonal water, and water outside myelinated axon, respectively. MacKay et al. (1994) published the first *in vivo* human study using multiple spin echo imaging to measure T_2 relaxation in white matter [55]. The multiple spin echo technique acquires 32 echoes at short intervals of 10 ms. They identified both short (T_2

= 10-40 ms) and long (T_2 = 70-100 ms) relaxation components, which were attributed to water between myelin bilayers and water inside and outside of the axon, respectively. From this, the myelin water fraction was defined as the ratio of myelin water signal to total water in a voxel. Subsequent studies using this approach demonstrated that myelin water fractions were positively correlated to myelin content in peripheral nerve, injury models, and post mortem tissue in healthy and diseased brains [38,56–58]. However, standard methods for quantifying this parameter are limited by long measurement times, low signal-to-noise ratio, and poor reproducibility [59,60].

Similar to T_2-based methods, multi-exponential behavior has also been observed in T_2* of white matter and has been recently developed to model *in vivo* myelin water fractions [61–64]. As mentioned, T_2* represents the combined effects of T_2 and T_2' and is sensitive to non-uniformities in the magnetic field. Non-uniformities often manifest as unwanted distortions, resulting in signal loss or artifact across an image. However, there are also non-uniformities at a sub-voxel level that arise from the magnetic susceptibilities of tissues [65]. Magnetic susceptibility refers to the ability of materials to become weakly magnetized (relative to water) when exposed to an external magnetic field (i.e., B_0) [66]. As hydrogen protons are sensitive to their magnetic environment, the observed MR signal, as measured with T_2*, will reflect the susceptibilities of the surrounding tissue. This property may offer unique insight for distinguishing the fast relaxing component attributed water associated with myelin, as the lipids and proteins of myelin are weakly diamagnetic (i.e., they faintly oppose the field). In addition, the orientation of myelinated fibers to the main magnetic field has been shown to influence the resonance frequency distributions of cellular water compartments. In a study by van Gelderen et al, investigators creatively demonstrated that the orientation dependence of fiber tracts was related to the anisotropy of magnetic susceptibility of white matter. For these experiments, a sample of

myelinated spinal cord was suspended in a strong magnetic field [67]. The orientation of the sample was turned by a fixed amount and measured for orienting effects, i.e., if the sample would reorient itself along the direction of B_0. This was indeed the case, and demonstrated that the sample had a preferred orientation to the magnetic field. The origin of anisotropic magnetic susceptibility is thought to correspond to the remarkably well-ordered structure of myelin due to the tight packing of lipid bilayers and the radial orientation of individual lipid molecules [64,68].

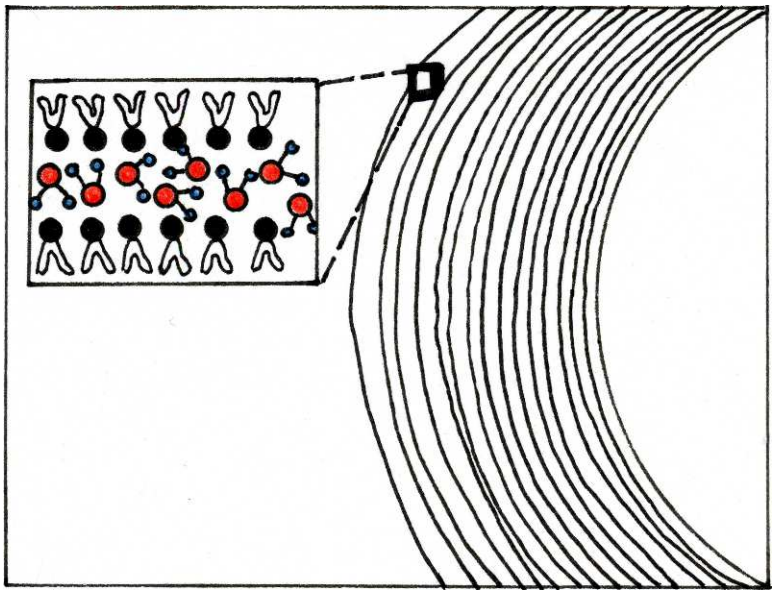

Figure 1.3 Water molecules between myelin bilayers. Myelin membranes are multi-layered, semi-permeable boundaries that functionally separate the axon from the extracellular matrix. While each layer is tightly compacted, water molecules exist and diffuse between layers. The diffusion of water is assumed to be slow relative to the time scale that MRI images are acquired. The rings are myelin wraps, and the inset box is water trapped between the outer surfaces of the phospholipid bilayers. The relaxation of myelin-associated water is fast relative to the relaxation of water inside the axon or in the extracellular space. Figure adapted from (water not to scale) [69].

In addition, myelinated axons are often assembled into coherent tracts, contributing to the macro- to micro-level organization of white matter. Most importantly, orientation dependence of magnetic susceptibility may be useful for extracting cellular-compartment information in myelinated tracts. For example, both theoretical and experimental studies have shown frequency shifts attributed to myelin water are larger for fibers perpendicular to the static field versus those in a parallel orientation [64,68].

Using a multi-echo gradient sequence (MGRE), both T_2* information and resonance frequency shifts can be acquired in white matter. The basic principles of multi-compartment modeling remain, where the relaxation of water in myelin layers is assumed to be fast relative to other water pools. The key differences are that these tissue parameters are sensitive the magnetic susceptibility of myelin composition and orientation of fiber tracts within the static field. The MGRE sequence acquires multiple echoes at very short spacing ~ 2ms. It has several advantages to the multiple spin echo sequence, such as reduced scan time, lower sensitivity to RF pulse inhomogeneities, and a low specific absorption rate (i.e., the amount of energy that can safely be applied to a person). These features allow for MGRE imaging of myelin water to easily translate to high magnetic field strengths where increases in MR signal help to distinguish between water compartments. Of note, this technique assumes that water is trapped and temporarily divided into three water compartments with distinct T_2* and frequency shifts: water within myelin layers, inside the axon, and in the extracellular spaces. This is due to the multiple wraps of lipid bilayers forming a semi-permeable boundary to the diffusion of water (Figure 1.3). As an analogy, imagine being trapped in a spiral maze made of tall, dense corn stalks. To get to your destination, you have two options: either stay on the path of the maze (easy), or plow through the dense corn stalks to skip to the other side. It would take time and energy to cross the layers of corn. Myelin

membranes are thought to slow the diffusion of water, but do not stop it completely. The time frame these data are acquired is assumed to be less than the time needed for a significant fraction of water to cross the myelin bilayers and mix with the surrounding pools. For this thesis, multi-compartment modeling of MGRE data will be tested for its utility as a relative estimate of myelin content in human brain.

1.2.3 Magnetization transfer imaging

The magnetization transfer (MT) approach is based on the assumption of two hydrogen proton pools. First, there are mobile hydrogen protons bound to water molecules (WP), i.e., the source of typical hydrogen-based MRI contrast. Second, there are non-water hydrogen protons bound to larger molecules, such as phospholipids of membranes, proteins, and other cellular constituents. Myelin is rich in lipids and proteins [70,71], and provides an abundant source of non-water, or macromolecular protons (MP). MPs are difficult to image directly, due to their extremely rapid relaxation times (50 μs < T_2 < 1 ms) [72]. To estimate the relative fraction of MPs, MT experiments assume the exchange of energy between each pool after a specialized RF pulse [73]. This "MT pulse" is used to saturate the MPs while minimally affecting the WPs. Over time, the MPs exchange their magnetization with the WPs, resulting in a decrease of observed T_1 contrast in tissue. The magnitude of this decrease is proportional to the type and volume of macromolecules contributing to MT effects.

The earliest example of this effect was shown in 1963, where investigators measured the exchange rate of chemical reactions [74]. A later published explanation proposed that there was cross-relaxation of water protons with non-water proton pools [75]. In 1989, Wolf and Balaban were the first to measure this effect *in vivo* using MRI, which became the basis for MT contrast.

In a typical MT experiment, there are multiple series of pulses to establish a fixed equilibrium, or steady state, in magnetization between the WP and MP pools. This technique has been shown as a sensitive measure for myelin content; however, it is highly dependent on sequence parameters, and can be susceptible to inconsistencies or errors across scanning sessions. In addition, steady-state MT techniques have long scan times when acquiring quantitative estimates of myelin content.

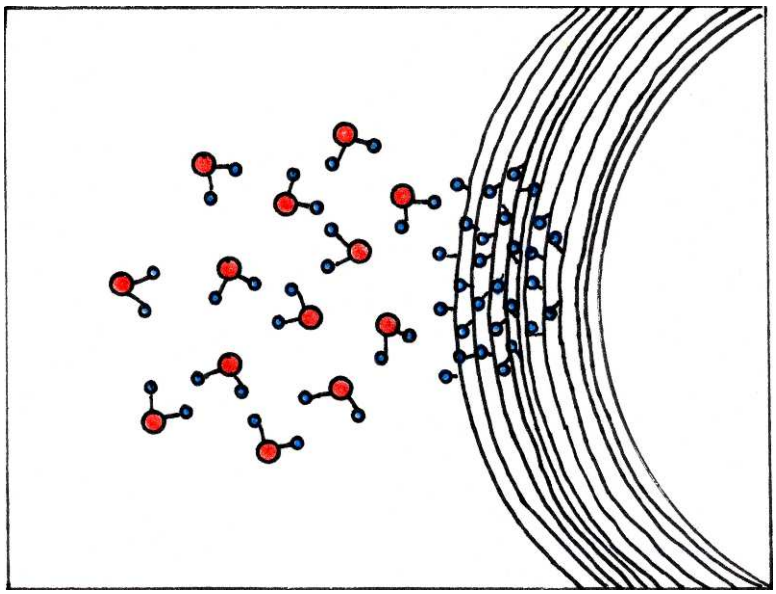

Figure 1.4 Water molecules and non-water protons bound to myelin. Schematic of hydrogen protons attached to water molecules (oxygen in red, hydrogen in blue) and non-water protons (hydrogen in blue) attached to myelin layers. The non-water, or macromolecular protons, are magnetized with a specialized RF pulse at the beginning of an MT experiment. The magnetization of macromolecular protons transfers to the water pool, which is imaged using MRI. Myelin membranes are a significant source of macromolecular protons throughout the brain, however, other membranes, proteins, and cellular structures also contribute to the non-water proton pool. Figure adapted from [76].

An alternate and faster approach is to measure the transient change in magnetization, by applying a single pulse, then acquiring imaging data at variable delay times after the pulse [74,77–79]. Each delay represents a different point in the equilibration of magnetization from MP to WP. As such, a two-pool model of exchange can be used to fit MP and WP signal evolution to extract an estimate of MP pool size and thus, an indirect measure of myelin content [74,80].

The myelin water and magnetization transfer imaging techniques described above offer novel opportunities for increased sensitivity for the MRI-based measurement of myelin in vivo. For this thesis, the reproducibility of each technique was assessed for application to a longitudinal study of adolescent development.

1.3 Adolescent development

Adolescence is a dynamic period characterized by physical, cognitive, and social maturation. The adolescent brain is inherently plastic to accommodate for typical growth and new experiences, but is also vulnerable to dysfunction [81]. Adolescence is the peak time for clinical onset of mental illnesses, many of which remain into adulthood [82]. Previous MRI studies have described a ~30% increase in white matter volumes, and ~ 8% increase in FA of white matter tracks from childhood to early adulthood [35,83,84]. White matter increases have been interpreted as the continued myelination of tracts and cortical regions throughout development. These regions are in part supported by oligodendrocytes that are increasingly complex (more extensions and less wraps) the later in life they differentiate [27]. These oligodendrocytes place high metabolic demands on the system, and are vulnerable to various disturbances. Myelin is necessary for optimizing the speed and synchrony of neuronal circuits; therefore, decreases or delays in myelin from typical patterns during adolescence are thought to coincide with cognitive dysfunction, or more seriously, mental illness [50].

From histological studies, we know later myelinating regions include areas important for multimodal integration, such as pre-frontal cortices and associated white matter tracts [11,32]. These studies are of great value due to the specificity to myelin; however, small numbers, static effects, and variability from the fixation process limit post-mortem results. The advent of MRI has been useful for comparisons of living human white matter. Unfortunately, standard techniques are insensitive to myelin, and there are mixed results as to the relationship of white matter, cognition, and genetic and physical factors, such as sex and puberty. Many studies include only small, cross-sectional samples, and could be improved using a longitudinal design. In this way, fewer subjects are needed to detect an effect, and can be related to change in age.

This thesis will investigate the application of a MRI-based myelin-sensitive approach to study longitudinal change in adolescent development. Characterizing typical myelin development as it relates to cognitive function is important for interpreting individual variability, and ultimately applying this information to elucidating mechanisms of dysfunction.

1.4 Thesis objectives

The remainder of this thesis focuses on testing the reproducibility of these techniques and whether they are ready for application to longitudinal studies of adolescent development. In Chapter 2, I examine the extent to which the MGRE method can be used on a clinical-strength MRI scanner by comparing the results of the method using two scanners (3 T and 7 T). This is of importance since clinical and research studies have begun to adopt this technique even though it has not been fully ascertained that the modeling is stable when the signal is acquired with a less powerful magnet. In Chapter 3, I compare the reproducibility of the MGRE method to the MT method in a cohort of healthy adolescents. It is important to establish the precision of each method, to select the best candidate for detecting underlying myelin content in tissue. For

Chapter 4, I apply the MT method to study longitudinal change myelin content during adolescent development. Finally, in Chapter 5, I provide an overall summary and conclusion regarding the use of these methods for future studies.

Chapter II. Comparison of gradient echo myelin water imaging at 3 and 7 tesla

2.1 Overview

Previous ultra-high field magnetic resonance imaging (e.g., 7 T) studies have demonstrated multi-exponential behavior of T_2* signal decay *in vivo* human white matter as attributed myelin, axonal and interstitial water compartments. While 7 T MRI has an inherent advantage of improved signal strength, 3 T is a more common field strength with greater potential for clinical and research applications. To evaluate the performance of this approach at 3 T versus 7 T, we acquired *in vivo* multiple gradient echo (MGRE) images to derive myelin estimates based on a multi-compartment T_2* relaxation model in four white matter regions of interest. Myelin estimates were less precise at 3 T than at 7 T; however, 7 T values were consistently lower than previous estimates of myelin content using similar techniques. This was unexpected, and unfortunately due to artifact during image acquisition. Simulations demonstrated 3 T fitting results were dominated by noise, and ultimately unreliable for separating axonal and interstitial component parameters. Constraining model parameters based on *a priori* information improved precision at 3 T, but led to inaccurate estimates of the myelin parameter. These results indicate that multi-compartment modeling of T_2* relaxation at 3 T is not sensitive enough to detect myelin-specific signal contrary to what much of the literature assumes.

2.2 Introduction

White matter in the central nervous system is comprised primarily of neuronal axons, many of which are tightly encapsulated by myelin sheaths. Myelin is made primarily of lipids and some proteins, and up to one-third of myelin thickness is due to water trapped between individual membrane wraps [30,71]. Myelin content changes throughout the lifespan, and is vulnerable to damage from metabolic insult in typical aging and various disease pathologies. As such, there is a strong clinical and research motivation to develop methodologies to quantify myelin content in the living human brain. The structural components of myelin membranes are difficult to image *in vivo* directly using MRI based techniques, as hydrogen protons of lipids and proteins have incredibly short relaxation times on the order of microseconds (50 μs < T_2 < 1 ms) [72]. To circumvent this challenge, MRI techniques have been developed to extract information that is unique to water compartments within and around myelin layers. The fraction of water within myelin layers (versus other waters) can be assessed and used as an estimate tissue myelin content.

MacKay et al performed the first *in vivo* human MRI experiments to estimate a myelin associated water fraction using a single-slice multiple spin-echo (MSE) MRI sequence [55]. Multi-exponential analysis of T_2 relaxation decay identified a rapidly relaxing myelin water component (T_2 = 10-40 ms) and a slowly relaxing, intra/extracellular water component (T_2 = 70-100 ms) [55]. Based on the relative amplitudes of these components, the "myelin water" fraction was estimated and proposed as a measure of myelin density. The traditional MSE sequence acquires T_2 decay curves across 32 echoes, with echo spacing of approximately 10 ms (range in echo times = 10 ms – 320 ms). The decay curves are then modeled with a nonnegative least squares (NNLS) fitting algorithm to estimate multi-component T_2 values and amplitudes. The NNLS algorithm makes

no assumptions as to the number water pools, although typically returns two to three components [55,60]. This approach has long been considered a gold standard in the field, as many studies have shown this parameter to correlate with histological measures of myelin content [56,58]. However, there is mixed consensus regarding the reproducibility of this technique [85,86], potentially due to the high sensitivity of NNLS model fitting to noise (low signal-to-noise ratio/SNR) and errors. Novel strategies have been developed to improve myelin water estimation, such as smoothing the T_2 distribution (regularization), or constraining the range of T_2 relaxation times for each water component [60,87]. In addition, sequences have been implemented to improve data collection, such as with fast whole-brain T_2 acquisitions [88], or for modeling different contrast mechanisms, such as multi-component fitting of simultaneously acquired T_1 and T_2 [89].

Similar to T_2-based methods, T_2* relaxation exhibits multi-exponential behavior in white matter and has been recently developed as a novel method for detecting *in vivo* myelin water fractions [61–64]. T_2* is comprised of both intrinsic T_2 and intra-voxel phase dispersions (T_2') induced by non-uniformities in the magnetic field. T_2' accelerates T_2 signal decay and its effects are intentionally reversed in MSE imaging to prevent bias and artifact from non-local field shifts (unwanted distortions). However, non-uniformities also exist at sub-voxel level that may offer unique insight into the cellular composition and structure of biological tissues. These tiny field distortions are generated from microscopic variations in the magnetic susceptibilities of certain tissues. Magnetic susceptibly quantifies the ability of materials to concentrate or distort a magnetic field [66]. The lipids and proteins of myelin weakly oppose the magnetic field, which contributes to the compartment-specific T_2* and frequency shifts (small offsets relative to the resonant frequency of hydrogen protons) observed in white matter. Susceptibly effects are also sensitive to the orientation of myelinated axons in the magnetic field. This may be due to the

unique molecular ordering of myelin, where membranes are tightly wrapped in compact layers with individual phospholipids orienting radially toward the axon. For example, fiber bundles oriented perpendicularly to the magnetic field have distinct compartment-specific frequency offsets, which almost completely disappear for parallel fibers [64]. Compartment-specific relaxation and frequency offsets can be measured using a multiple gradient echo (MGRE) MRI sequence. MGRE images are obtained with a short first echo time and narrow echo spacing [63,64]. Each echo time provides a complex image of the amplitude and phase corresponding to T_2* relaxation. The phase is filtered to remove non-local effects (i.e., unwanted distortions due to susceptibility differences), and results are analyzed by fitting a three component multi-exponential model to the complex data. In contrast to NNLS, this model assumes a fixed number of pools for myelin water, axonal water, and interstitial water. The three-pool model is based on numerous *in vivo* and histological experiments, and may infer useful information for characterizing non-myelin water components [60].

MGRE MRI has several notable advantages to the MSE approach. First, scan times are shorter and allow for higher spatial resolution. MGRE is also less sensitive to radiofrequency (RF) pulse inhomogeneities and has a lower RF power deposition. As such, MGRE can easily translate to high magnetic field strengths (e.g., 7 T) to benefit from improved SNR and tissue contrast [90,91]. In particular, high field MGRE imaging has increased susceptibility contrast, and thus, higher likelihood of accurate parameter estimation [64]. Unfortunately, MGRE is also more sensitive to non-local field disturbances. While certainly not limited to high field, these effects are more pronounced at 7 T than 3 T. Some notable issues include field fluctuations due to respiration [92], large differences in susceptibility values near air-tissue boundaries causing wider signal loss/dropout, sensitivity to static field distortions at the start of an experiment, and

unexpected shifts in the magnetic field due to gradients being quickly pulsed on and off (e.g., eddy currents) [62].

Studies of MGRE-based myelin water estimation have been previously investigated at both 3 and 7 T using complex data. While 7 T benefits from improved SNR and susceptibility contrast, it is currently unclear if the 3 T application of this method is sufficient to resolve each water compartment. As this technique becomes more widely available, it is relevant to test the feasibility of multi-compartment fitting at the clinical field strength of 3 T. For this project, we will investigate whether or not myelin, axonal, and interstitial water compartments can be adequately resolved at both 3 T and 7 T field strengths and investigate their relative advantages. To test this, MGRE data were acquired in healthy adult participants at both field strengths. In addition, we used numerical simulations to evaluate model performance for both field strengths.

2.3 Methods

2.3.1 Participants

One group of healthy adults was scanned at 3 T (n=8 females, n=7 males, ages 21-49, mean age 28.4) and another at 7 T (n=9 females, ages 23-49, mean age 30.5) scanners (Siemens 3 T Skyra or a Siemens 7 T; Erlangen, Germany) using 32-channel receive-only RF coil arrays. Four female participants were imaged as part of both groups. Three participants were excluded from analysis due to artifacts that occurred during acquisition (n=2, 3 T; n=2, 7 T). Participants had no reported history of neurological or psychiatric illness. All participants provided informed consent in accordance with the Institutional Review Board of the National Institutes of Health.

2.3.2 MRI acquisition

A custom MGRE sequence [63] was developed to map the evolution of the amplitude and phase components of T_2* signal decay over time. At 3 T, 30 positive-only echoes were collected with echo times (TEs) ranging from 3.3 to 58.2 ms and an echo spacing of 1.92 ms. At 7 T, 38 positive-only echoes were collected with TE ranging from 2.3 to 62.7 ms and an echo spacing = 1.6 ms. Both 3 T and 7 T used the same parameters for repetition time (TR) = 1,000 ms, voxels with an isotropic resolution of 1.5 mm^3, and bandwidth set to 250 kHz. The flip angle was either 60° or 70° for both field strengths. Nine to fifteen slices were acquired in axial orientation, coplanar with AC–PC to cover the corpus callosum. Most scans were repeated five times, with the exception of two 3 T scans that had only three repetitions. The total scan time for all five repetitions was 10 minutes (i.e., 2 minutes per repetition).

2.3.3 Data processing

Complex-valued images were generated to provide an amplitude and phase at each voxel for each echo time. The phase images were preprocessed in two steps to remove non-local susceptibility effects. First, a linear phase offset term (φ) was calculated over time (TE) and subtracted from each voxel included in the analysis. Second, to correct for eddy-current effects, a whole slice phase map was calculated for each echo independently to remove spatially linear phase variation. A single rater (E.P.R.) visually inspected all repetitions for remaining artifact or motion distortion. Anterior regions were more sensitive to field inhomogeneities, due to susceptibility distortions based on their proximity to air-tissue interface (e.g., around the sinuses). SNR was measured from the first echo and first repetition of the magnitude images, and

divided by the square root of a pre-scan noise measurement. After phase correction, scan repetitions were averaged to improve SNR and stability.

Four white matter regions of interest (ROIs) were manually drawn on magnitude images at TE=60 ms (3 T) and TE=43 ms (7 T) to optimize gray and white matter contrast. ROIs included a bilateral optic radiation (OR), splenium (SCC) and genu (GCC) of the corpus callosum, and a bilateral mid-frontal white matter region (FLWM) (Figure 2.1). These regions were selected to be perpendicular to B_0 to minimize variability due to the orientation dependence of myelinated fiber tracts [64,67,68]. ROIs were drawn across three contiguous slices, and signal was averaged across all voxels and slices for each ROI. Due to the limited slice coverage, the OR was not present on one scan at each field strength (3 T, 7 T).

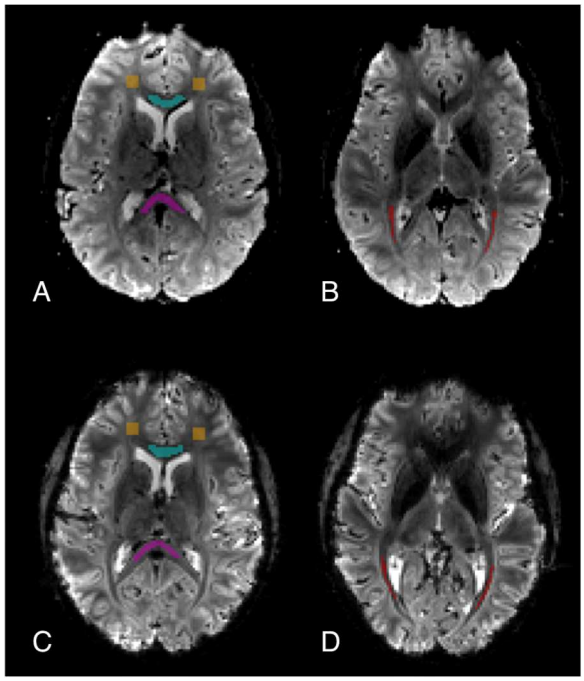

Figure 2.1 Region of interest selection on T_2*-weighted magnitude images. Regions were defined on T_2*-weighted magnitude images at 3 T (30th echo, TE=60 ms) (A, B) and 7 T (25th echo, TE=43 ms) (C, D). Starting from the most posterior region, ROIs included OR (red), SCC (magenta), GCC (turquoise), and FLWM (orange). OR was typically ventral (inferior) to the other three regions.

2.3.4 In vivo analysis and parameter estimation

Signal decay curves (amplitude and frequency shift) were compared between the two groups acquired at different field strengths for each of the four ROIs (Figure 2.2). The signal amplitude represents the apparent T_2* signal intensity measured at each echo time from the magnitude images. After filtering out nonlocal field effects, the frequency shift was calculated as the change in phase over time, and represents the nonlinear shift in mean resonance frequency (relative to water). These signals are sensitive to compartment-specific changes in susceptibility, which can be observed even prior to complex model fitting. For example, white matter fiber tracts that are perpendicular to the main field have faster T_2* relaxation at later echoes (measured by the apparent loss of signal amplitude); whereas frequency shifts have rapid, initial offsets within the first 10 ms of the experiment. This nonlinear evolution in frequency shift is of particular interest, as it does not represent the pattern seen in nonlocal effects (i.e., unwanted distortions) that tend to vary linearly with echo time. The nonlinear shift in frequency is thought to relate to microstructure, and in particular the magnetic susceptibly of myelin composition and molecular ordering.

$$S = (A_1 e^{(-R_{2,1}^* + i2\pi\Delta f_1)t} + A_2 e^{(-R_{2,2}^* + i2\pi\Delta f_2)t} + A_3 e^{-R_{2,3}^* t}) e^{i(2\pi f_g t + \varphi)} \quad [1]$$

A three-component model was fit to complex-valued signal (S), where *i* was the imaginary unit, A_n the amplitude, $R_{2,n}^*$ the relaxation rate, Δf_n the frequency shift calculated as relative to global/interstitial frequency, f_g, and φ the phase offset. Components 1, 2, and 3 correspond to myelin, axonal, and interstitial water, respectively. Previous experiments [63,93] were used to define "first guess" starting values for nine parameters to initiate model fitting (Table

2.1, INIT). The interstitial water frequency shift was assumed to be on resonance and set to 0 Hz. The initial starting values do not directly correspond to ROI-based estimates modeled in these data, but help to refine the otherwise slow optimization process during subsequent steps. The initial search range was ±30% from each first guess value (INIT), then optimized over a series of iterations (search range = ±30%) that refined every component by minimizing the sum of squares of the residue of the fit for a given range of its parameters [63]. The search was limited to positive values for the amplitudes and relaxation rates. Model optimization was terminated once residues could no longer be reduced. To account for the lower signal strength (and thus lower signal-to-noise ratio) of echoes at increasing TE, the signal amplitude was used as a weighting factor to prioritize early echoes. Subject-averaged model parameters are reported for each ROI. To investigate differences in model performance at each field strength, we reported ROI-averaged model descriptors, such as goodness of fit and root-mean-square error (RMSE), in addition to voxel-wise SNR and tissue volumes. And finally, we compared the multi-exponential and mono-exponential (individual components) fitting results and model residues for a single volunteer scanned at both field strengths. The residues are a visual representation of model error (fit-data) over echo time. Large, or systematic deviations in the residue indicate certain signal characteristics are not captured by the model, such as susceptibility contributions, or even nonlocal effects from field distortions.

2.3.5 Numerical simulations

Simulations were performed to investigate the influence of noise on the precision of model performance for each field strength. Complex-valued T_2* decay signals (using Eq. 1) were generated from tissue parameter sets acquired previously from human subjects at 3 T and 7 T

(see Table 2.1). These parameter sets corresponded to the average values of the four white matter ROIs: OR, SCC, GCC, and FLWM. Gaussian noise was added incrementally to the simulated input data at 0.1%, 0.2%, 0.3%, and 0.4% of the total signal. The lowest noise level (0.1%) was selected to approximate ROI-averaged noise levels from the experimental data (3 T = ~ 0.1%, 7 T = ~ 0.05%). The three-compartment model was applied to each realization of added noise. This was repeated 1,000 times for each ROI parameter set for each level of noise. The extracted myelin amplitudes ($A_{1,\,sim}$) were compared to a "ground truth" value, i.e., the myelin amplitude used in generating the T_2* signals ($A_{1,\,tiss}$). Deviations from the ground truth ($A_{1,\,tiss}$) represent error in model fitting. For each field strength, we examined 1) the accuracy of $A_{1,\,sim}$ when no noise (0%) was added to the input signals, and 2) the relative magnitude and bias of errors for $A_{1,sim}$.

Constraining some model parameters to *a priori* values can improve precision of the freely fit parameters, but may introduce bias in the parameter(s) of interest. Nonetheless, this can be advantageous in situations where either the constrained parameter is insensitive to model fitting (and can be ignored with only small penalties), or the parameter of interest (A_1) is minimally affected by these errors. Either way, multi-exponential models are complex, and thus susceptible to noise and error propagation during fitting. To reduce the complexity of the ten-parameter model and test for improvements in precision of myelin estimates, we repeated noise simulations (1,000 realizations for four ROIs, at four noise levels) while holding either axonal (A_2) or interstitial amplitudes (A_3) at their initial starting values (Table 2.1, INIT). Even though amplitudes are highly correlated (i.e., an increase in A_2 will result in a decrease in A_3), either value may influence myelin water estimation (A_1) to a different extent.

Multi-exponential fitting of 7 T data has an inherent advantage over 3 T due to enhanced susceptibility contrast and higher SNR. To confirm this and compare model performance between field strengths, we constrained parameter estimates to incorrect values during the fitting routine. No noise was added to these data in order to isolate contributions from individual parameters. When including incorrect values, there should be increased error (i.e., the difference of model fit and simulated data), which varies depending on the sensitivity of each parameter during the fitting process. The root-mean-square error (RMSE) was calculated for each trial to represent the magnitude of error for each incorrect value. RMSE was expected to scale relative to the magnitude of the inaccuracy in the parameter estimate (i.e., a larger deviation from the true value would result in a larger error), but it was unknown what the magnitude of the error might be between field strengths, and which parameters were the most/least sensitive to these deviations. Noise-free, complex-valued T_2* decay signals (using Eq. 1) were generated from the ROI-averaged SCC tissue parameter set at 3 T and 7 T (see Table 2.1). The SCC was selected for these simulations, as it has been previously used as a model region for multi-exponential modeling in white matter. SCC is an easily defined tract, and located far from susceptibility artifacts due to the anterior sinus cavities. The ROI-averaged SCC tissue parameter sets (i.e., the same values used to generate the signal) were used as initial starting conditions. Therefore, model fitting was able to compute the exact solution when allowing all parameters to freely fit the data (no constraints). The deviations in parameter estimates were calculated in small increments of ± 2.5% from the true value, up to a maximum of ± 15%. One parameter was fixed per simulation, and the RMSE was calculated for each trial. The f_g and φ were not included for these simulations as they were assumed to be at or near on-resonance throughout the experiment.

2.4 Results

2.4.1 In vivo analysis

Signal amplitude decay was similar for all fiber tracts, with only small deviations seen in later echoes (~ TE=20 ms) at 7 T. For the group scanned at 3 T, amplitude decay was slower and frequency shifts were smaller, consistent with the reduced effects of susceptibility variations on the T_2* signal. The FLWM region had the smallest frequency offset for both field strengths. While all ROIs were selected to be perpendicular to the main field, the FLWM funnels inputs from several prefrontal cortical areas, and may have less defined fiber orientation relative to the compact tracts of SCC, GCC, and OR. This study did not acquire diffusion tensor imaging to confirm the orientation of fiber bundles to the magnetic field; thus, differences in head positioning may partially contribute to between subject variance at each echo time. The most notable and unexpected finding, however, was that frequency differences for 7 T had extremely high variance at each echo time compared to the group at 3 T. When examining the phase data, these images had periodic, wave-like artifacts (like a wiggle) throughout all scan repetitions and subjects. The periodicity and amplitude of the artifact was semi-irregular, making it difficult to correct for during image processing. Different image resolutions (1 mm^3, 1.5 mm^3, 2 mm^3) were examined to mitigate this effect, but it was present throughout (data not shown).

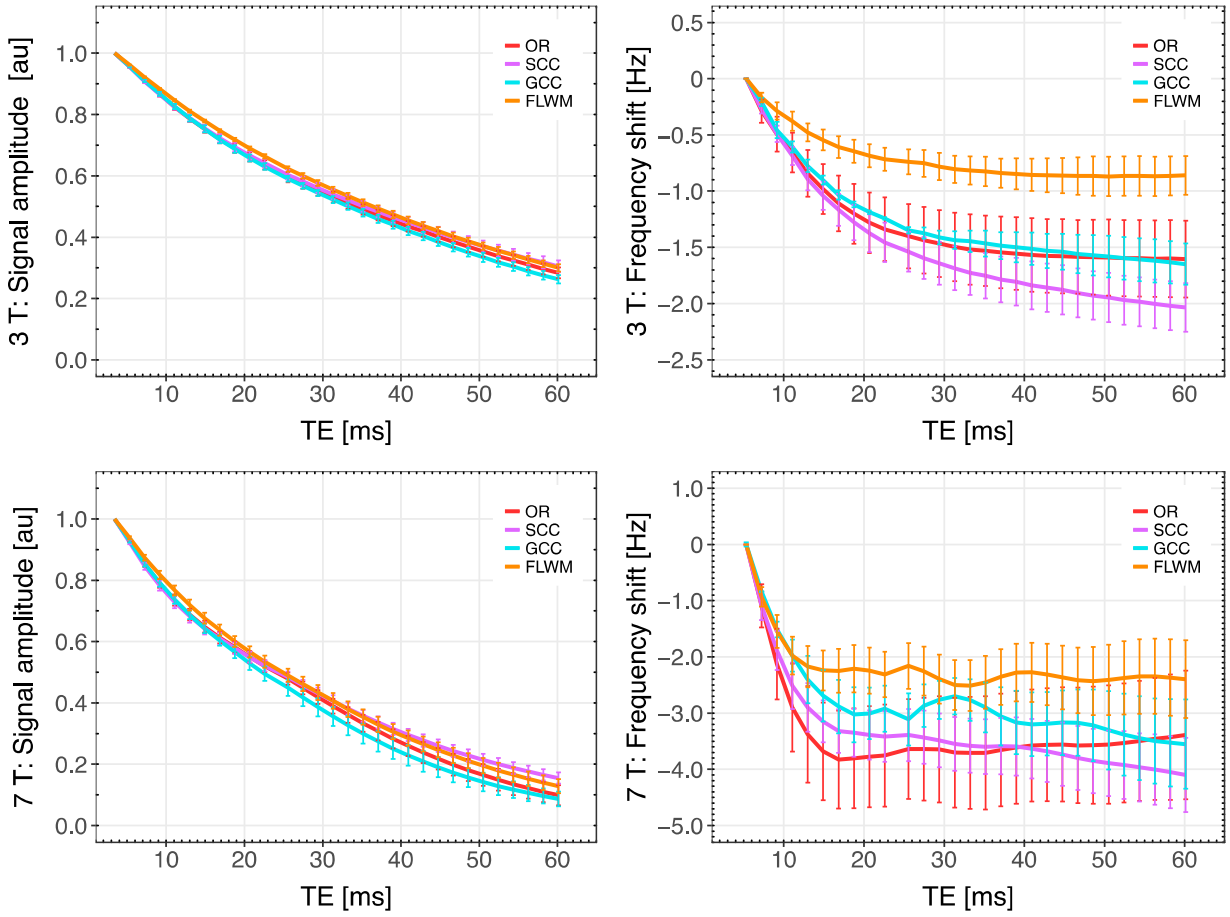

Figure 2.2 Subject-averaged amplitude and frequency curves. Normalized signal amplitude (A, C) and frequency shifts (B, D) in four white matter ROIs averaged over all subjects. Error bars denote standard deviations. Frequency differences were calculated as the change in phase evolution over echo time where TE_0 (3 T = 3.4 ms; 7 T = 2.3 ms) was used as reference. Frequencies were shifted to start at 0 Hz to observe the relative change in each ROI. The y-axis is set to different values for panel B and D to distinguish small differences in frequency shifts between regions.

Average parameters for 3 T and 7 T data are presented in Table 2.1. Amplitudes were defined as the relative fraction of each water compartment to total water, and can be directly compared for groups scanned at different field strengths. Larger R_2* values indicate shorter T_2* relaxation times, with increases in R_2* assumed to be approximately linear to increases in field strength. Frequency shifts are also greater at 7 T (see Figure 2.2; B, D), but were converted from Hertz to parts per million (ppm) to compare between field strengths (Table 2.1).

Table 2.1 ROI-based fitting results of the three-compartment model. Initial starting conditions (INIT) were determined from previous experiments in SCC (7 T) and assumed to be appropriate for 3 T as well (adjusting for field strength). Mean (Av) and standard deviation (SD) of three-component fitting results are shown for four white matter ROIs. A_n is the relative amplitude (%), $R^*_{2,n}$ the relaxation rate (Hz), and f_n the frequency shift (ppm) of component n. Myelin and axonal water frequency shifts were adjusted relative to a global/interstitial water frequency set to 0 ppm. The OR was not present for two subjects because slice positioning was too high.

				Myelin			*Axonal*			*Interstitial*	
B_0	N	ROI		A_1	$R^*_{2,1}$	Δf_1	A_2	$R^*_{2,2}$	Δf_2	A_3	$R^*_{2,3}$
3 T	-	INIT		16	80	0.08	43	20	-0.03	41	24
	13	OR	Av	12.1	81.0	0.08	39.0	13.8	-0.05	51.3	18.4
			SD	*2.0*	*4.5*	*0.01*	*2.5*	*1.0*	*0.004*	*2.1*	*1.1*
	14	SCC	Av	13.8	82.7	0.06	52.3	11.4	-0.06	36.2	20.2
			SD	*2.9*	*5.6*	*0.01*	*7.5*	*1.5*	*0.007*	*5.4*	*2.5*
	14	GCC	Av	10.0	74.5	0.08	44.9	13.9	-0.06	47.3	20.2
			SD	*3.8*	*13.2*	*0.03*	*9.0*	*2.2*	*0.008*	*7.3*	*2.5*
	14	FLWM	Av	8.7	68.9	0.08	39.1	15.4	-0.04	54.1	17.5
			SD	*5.5*	*14.4*	*0.03*	*4.1*	*1.5*	*0.007*	*5.9*	*3.3*
				Myelin			*Axonal*			*Interstitial*	
B_0	N	ROI		A_1	$R^*_{2,1}$	Δf_1	A_2	$R^*_{2,2}$	Δf_2	A_3	$R^*_{2,3}$
7 T	-	INIT		16	160	0.07	43	24	-0.02	41	38
	6	OR	Av	8.6	123.0	0.12	23.4	24.1	-0.03	70.3	35.3
			SD	*1.7*	*21.4*	*0.02*	*5.7*	*4.3*	*0.003*	*5.2*	*3.7*
	7	SCC	Av	12.2	158.9	0.08	45.8	24.4	-0.04	45.1	40.3
			SD	*1.2*	*9.8*	*0.01*	*6.7*	*2.0*	*0.004*	*6.9*	*2.5*
	7	GCC	Av	4.3	81.9	0.10	34.7	30.2	-0.04	63.3	41.8
			SD	*2.1*	*40.4*	*0.04*	*5.6*	*5.6*	*0.003*	*4.1*	*3.2*
	7	FLWM	Av	5.6	151.4	0.09	28.8	25.8	-0.03	67.7	35.6
			SD	*1.5*	*22.6*	*0.02*	*11.8*	*4.9*	*0.002*	*12.0*	*4.0*

All participants were healthy adults, and had no indications of white matter abnormalities when participating in this study. As such, we expected amplitudes to have similar ROI-based estimates between field strengths. This was not the case, as 7 T had consistently lower A_1 and A_2, (thus higher A_3), for each ROI measured. In particular, average A_1 values for GCC and FLWM were ~ 5% at 7 T. The 7 T GCC also had significantly low R_2* values for the myelin component, indicating this region was unreliable for detecting the myelin component. At 3 T, A_1 was more consistent between regions, but had a two-fold higher variance than the group scanned at 7 T. In addition, the assignment of axonal and interstitial amplitudes was not consistent for 3 T data. For example, the average SCC had increased A_2 relative to A_3, while OR, GCC, FLWM had decreased A_2 relative to A_3. These differences might indicate poor sensitivity in differentiating between each compartment. At 7 T, SCC had similar results for these components, however, A_2 was significantly lower than A_3 for OR, GCC, and FLWM.

To examine the characteristics of the model fit in more detail, we examined myelin, axonal, and interstitial results and model residues over echo time. We chose the SCC for this comparison since it is expected to have the most consistent results. This comparison was limited to one subject that was scanned at both field strengths. As seen in Figure 2.2, amplitude decay was slower at 3 T, which corresponded to the smaller susceptibility effect of signal at 3 T. Model residues were small at both field strengths, (scaled 100x), however, a systematic deviation was observed in early echoes at 7 T [63]. This non-random pattern of model residues was also observed in OR, GCC, and FLWM across all volunteers at 7 T. These errors were reflected in the composite metrics of model performance shown in Table 2.2, even as 7 T data had twofold higher SNR as compared to 3 T.

Table 2.2 ROI-based volumes, signal-to-noise ratios and model performance indices. Mean and standard deviation (SD) are reported for each ROI volume, as well as voxel-wise SNR, goodness of model fit (1-R^2), and the ratio of RMSE to noise level. RMSE can also indicate goodness of fit, and was contrasted with ROI-averaged image noise as a ratio. The OR was not present on two subjects because slice positioning was too high.

B_0	N	ROI	Volume, mm^3	SNR	1-R^2 (E-04)	RMSE/noise
3 T	13	OR	439.0 (77.7)	90.2 (9.3)	0.11 (0.03)	1.1 (0.2)
	14	SCC	680.6 (203.3)	75.9 (6.8)	0.12 (0.03)	1.2 (0.2)
	14	GCC	482.1 (74.3)	78.6 (5.7)	0.27 (0.14)	1.5 (0.3)
	14	FLWM	467.2 (72.4)	92.2 (8.4)	0.09 (0.04)	1.1 (0.3)
7 T	6	OR	344.8 (119.9)	228.6 (12.2)	2.25 (2.44)	7.6 (5.1)
	7	SCC	619.1 (123.6)	191.7 (11.3)	0.62 (0.16)	4.9 (0.8)
	7	GCC	463.8 (117.0)	209.4 (9.8)	2.85 (3.29)	8.4 (3.6)
	7	FLWM	495.2 (94.9)	228.7 (12.5)	1.31 (0.88)	7.5 (2.1)

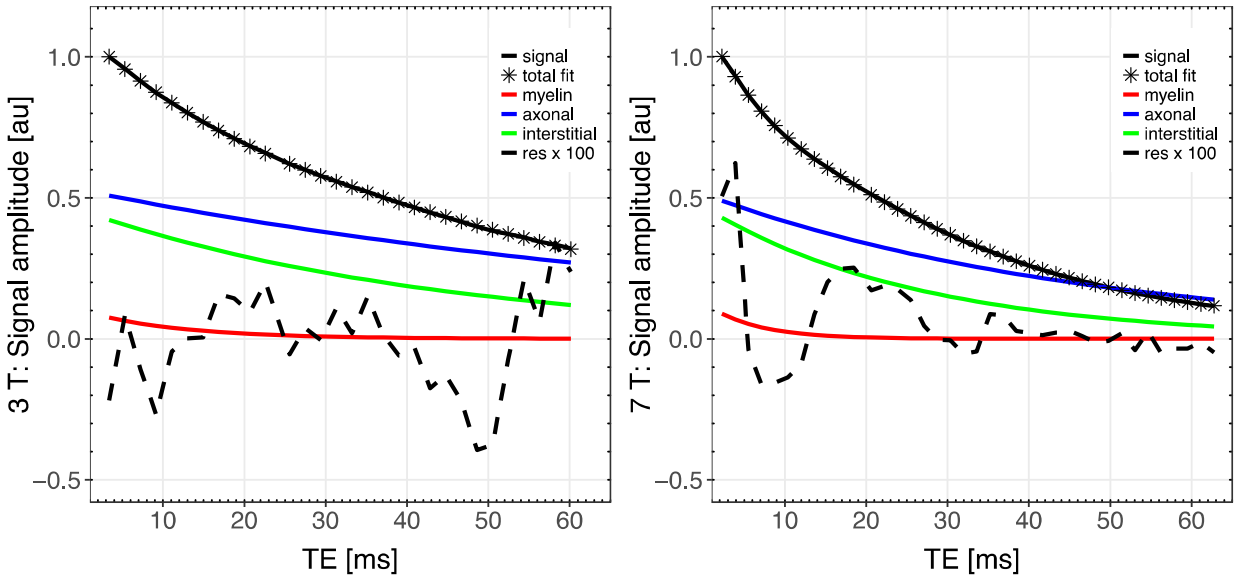

Figure 2.3 Amplitude decay curve and multi-exponential fit for one volunteer. Three-compartment model fit results (symbols) of normalized signal amplitude (lines) in SCC for one volunteer at 3 T (A) and 7 T (B). Model residue, scaled by 100 (res x 100) is overlaid for each plot (dashed line). Mono-exponential fit results are shown for myelin (red), axonal (blue), and interstitial (green) compartments. A noticeable non-random pattern is observed in the 7 T residues.

2.4.2 Numerical simulations

Figure 2.4 shows the percent difference of simulated myelin water amplitudes versus expected tissue values for each level of added noise. Noiseless data demonstrated model fitting for all tissue parameter sets was highly accurate at 7 T, (<1% difference), even when including clearly deviating R_2^* values for GCC. For 3 T, A_1 estimation was inaccurate, which was most apparent within the range of experimental noise levels (0% and 0.1% added noise). The 3 T myelin estimates were two times more variable than for 7 T (Table 2.3), indicating 3 T values may be dominated by noise in experimental conditions. As such, 7 T data were more accurate and reproducible for each ROI.

Additionally, interstitial and axonal water amplitudes (A_2, A_3) were held constant at their initial starting values during model fitting to test for potential improvements in precision of A_1. While there were small reductions in variance at 3 T, myelin amplitudes were overestimated for each set of ROI parameter values (see Supplementary Table 2.S1). At 7 T, fixing A_2 and A_3 did not reduce variance, while again A_1 was overestimated for each parameter set. Thus, these simulations showed some gains in precision only at 3T, especially for the 0.3 - 0.4% noise levels, but at both field strengths fixing these parameters negatively affected A_1 estimation.

Table 2.3 Variance in myelin parameter estimation due to noise. The SD (absolute and relative percentage) of myelin water amplitudes (A_1) for simulated data with increasing levels of noise.

		0.01%		0.02%		0.03%		0.04%	
B0	ROI	SD	SD (%)	SD	SD (%)	SD	SD (%)	SD	SD (%)
3 T	OR	1.3	9.9	2.5	19.4	3.8	27.1	5.0	35.6
	SCC	1.3	9.0	2.5	17.7	3.8	26.8	4.9	35.0
	GCC	1.1	11.1	2.3	20.6	3.5	31.9	4.7	42.6
	FLWM	1.5	15.4	2.9	28.8	4.0	40.3	5.1	51.0
7 T	OR	0.3	3.0	0.6	6.1	0.9	9.1	1.3	12.4
	SCC	0.8	5.6	1.4	10.5	2.0	14.9	2.6	18.9
	GCC	0.2	4.0	0.4	8.2	0.6	12.4	0.8	17.0
	FLWM	0.5	8.7	1.1	17.4	1.7	26.1	2.3	34.9

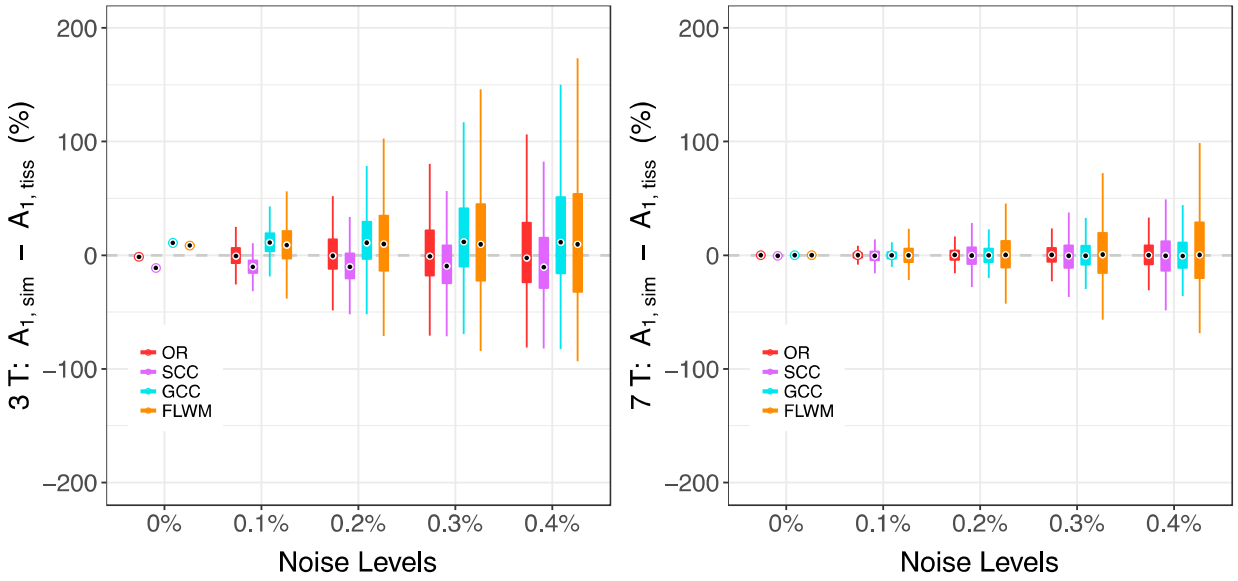

Figure 2.4 Distribution of myelin water amplitudes due to noise. Tissue values obtained from *in vivo* experiments (Table 2.1) were used in the forward model (Eq. 1) to test fitting accuracy under conditions of additive noise for 3 T (A) and 7 T (B) data. Percent differences in myelin water amplitudes (A_1) were calculated for simulation results ($A_{1,sim}$), versus expected tissue values ($A_{1,tiss}$). Each box plot marks the median (dot), the 25-75% inter-quartile range (box), and the full data range (line). The dashed horizontal line (grey) on each plot corresponds to 0% difference, or in other words a perfect fit. Each color corresponds to a different ROI.

Fitting errors, as reported by RMSE, were used to indicate the sensitivity of individual parameters when constrained to incorrect values (Figure 2.5). Therefore, high RMSE values were preferred, indicating fitting was more sensitive to inaccuracies (i.e., the fixed, incorrect value). For low RMSE values, individual parameters were deemed insensitive, as multiple values could be used to produce similar solutions with no penalty. This is a dangerous scenario, as incorrect estimates contribute to inaccuracies in the parameter of interest (A_1). In Figure 2.5, constraining 3 T A_1 to +15% of its expected value (i.e., $A_{1,+15\%}$=16.3), resulted in an increase in RMSE from baseline (leftmost graph in Figure 2.5, A). The same parameter increase of +15% in A_1 for 7 T simulations resulted in a larger increase in RMSE (relative to 3 T). These results indicate 7 T model fitting was more sensitive to the perturbation of an inaccurate solutions (the fixed +15% change in A_1) over 3 T, and should provide better estimates of A_1. Most notably for 3 T, the axonal and interstitial components were insensitive to changes in these fixed parameters. Sensitivity did improve when fixing an additional parameter, A_3 for example, for all model parameters at both 3 T and 7 T.

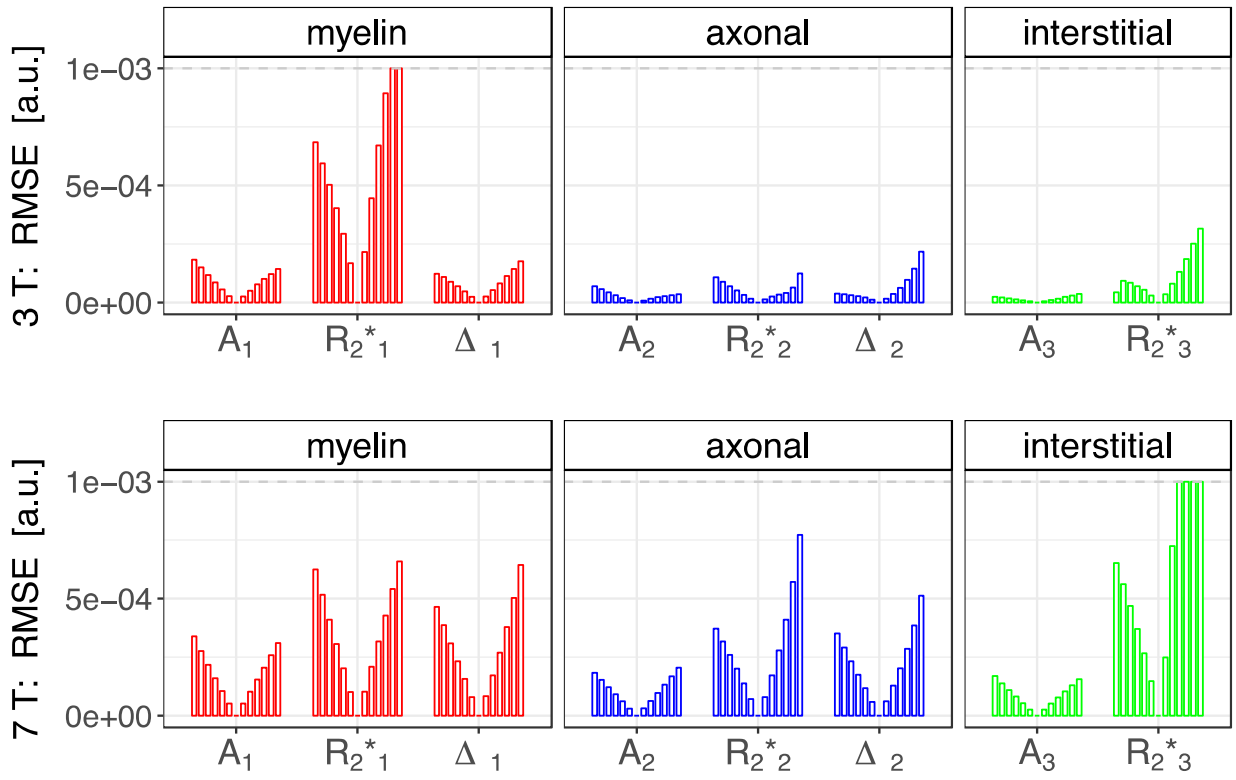

Figure 2.5 Residual fitting error when using incorrect parameter estimates. Bar plots of 3 T (top) and 7 T (bottom) RMSE generated while constraining individual starting parameter values during model fitting. For each parameter, values were scaled in steps of up to ± 15%. The dashed horizontal line (grey) on each plot corresponds to a 0.1% noise level.

2.5 Discussion

This study compared the performance of a three-component model using T_2* decay curves at 3 T and 7 T. The MGRE-based approach benefits from high field field strengths due to increased SNR and susceptibly effects; thus, the 7 T results were used as a benchmark to compare the application of this method at 3 T.

From the *in vivo* experiments, myelin amplitudes were up to four times more variable for 3 T; however, average 7 T myelin amplitudes (A_1) were surprisingly low, ranging from 4.3 to 5.6% in anterior brain regions. A previous study at 7 T reported T_2*-based A_1 values in

demyelinating lesions to be ~3-4 % versus posterior white matter tracts of ~10-15 % [93]. In addition, T_2-based studies typically report ~10-15% myelin water fractions across various white matter tracts [94]. As such, the 7 T myelin amplitudes from these data were considered unreasonable estimates of myelin content for healthy adult volunteers.

There are several potential causes of low A_1 values at 7 T, in addition to the large difference in variance between groups. First, anterior regions are difficult to image using T_2*-based techniques due to signal loss near the anterior sinus cavities. In addition, these artifacts increase linearly with field strength, and may contribute to unwanted variability in myelin estimates. This was apparent at 3 T, where standard deviations of A_1 were increased for anterior (GCC, FLWM) relative to posterior brain regions (OR, SCC). However, 7 T A_1 values had similar variance across all four ROIs. Thus, 7 T myelin amplitudes were consistently low versus 3 T, yet less likely to be influenced by noisy data due to susceptibility artifacts. Another explanation for differences in A_1 is that the three-compartment model may not completely describe signal behavior. There was evidence to suggest this for 7 T fitting, as Figure 2.3 showed a small, yet systematic residue for early echo times whereas 3 T had no such effect. T_2* signal decay is much faster for 7 T (versus 3 T) due to the increased susceptibility effects of myelin at high field strengths. There are limits, however, to how many echo times (data points) can be acquired to capture these transient effects. As such, fewer data points are available for model fitting at 7 T, which may introduce unwanted variability in parameter estimation. A final possibility related to differences in A_1 is related to measurement errors during image acquisition. The phase of the 7 T MRI data had wave-like artifacts that were indicative of eddy currents. Eddy currents were most likely caused by the miscalibration of scanner gradients, which could not be adequately corrected for during image pre-processing. As such, we were unable to

conclude if model performance or eddy currents were the primary cause of differences in myelin amplitudes at each field strength.

To further investigate the performance of the T_2* approach, we also performed simulations to assess the precision and accuracy of myelin estimation. Parameter estimates at 3 T were highly susceptible to even low levels of noise, having a twofold greater dispersion of data points versus 7 T. In addition, noiseless conditions produced inaccurate myelin estimates for 3 T data. We determined this to be true for multiple combinations of parameter sets, indicating the model was unreliable for resolving three components at 3 T. Inaccurate estimates of A_1 were likely due to the fitting routine getting stuck in a local minima, which could not be resolved even with unlimited SNR. At higher noise levels, the randomness and increased amplitude of Gaussian noise effectively masked the erroneous A_1 distribution. This was partially offset by holding the axonal or interstitial amplitude constant, at which point the model fit was better able to discriminate among the three water compartments at 3 T. While this afforded some benefits, myelin amplitude estimation was less accurate. Even so, fixing this parameter could still be an improvement in the separation of the myelin and axonal components.

Novel methods for physiological noise correction (i.e., respiration and cardiac pulsation) may improve the quantification of multi-compartment modeling in anterior brain regions [95]. Another strategy to improve myelin water estimation would be to acquire full-brain coverage and reduce slice spacing and thickness. While this would increase scan time with the current technique, recent work has shown that this can lead to a reduction in errors using susceptibility mapping techniques [96].

2.5.1 Conclusions

This study investigated the performance of fitting a three compartment model to T_2* signal decay at 3 T and 7 T. Data simulations revealed myelin estimates at 3 T were hampered by noise, and ultimately insensitive to separating axonal and interstitial compartments. The 3 T simulations were improved by constraining selected model parameters to predefined values, but also introduced new errors in myelin amplitudes. These results strongly suggest that caution should be used when applying these techniques at 3 T.

Chapter III. Reproducibility of novel myelin water and magnetization transfer imaging methods

3.1 Overview

Myelin water (MW) imaging and magnetization transfer (MT) imaging are MRI methods with purported specificity to myelin content in white matter. As such, these methods have been widely applied to assess myelin pathology in humans and animal models. Previous studies have evaluated MW and MT imaging performance in detecting myelin; however, new developments in sequence design and tissue modeling require further investigation into their use and application. For this study, we compared the reproducibility of novel MW and MT imaging methods in a cross-sectional cohort of 93 healthy adolescents, ages 12.7 – 16.8. Multiple repetitions of each scan type were acquired during a single scanning session to determine the reproducibility of myelin parameters in four white matter regions of interest. Prior to model estimation, MW and MT imaging data were compared to examine the level of variability resulting from measurement noise. The within scan variance (pooled across all repetitions for all subjects) was 0.5-1.0% for MW and 1.0-1.5% for MT, with anterior ROIs having the highest variance regardless of method. Thus, MW input signals were more precise (thus, more reproducible). For model estimation, the MW-derived myelin parameters (f_{MW}) extracted from experimental data were up to ten times more variable than the MT parameter (f_{MT}). To investigate the large difference in variance between fitted parameters, MW and MT data were simulated to test the impact of measurement noise on parameter estimation. These results indicated the variability in f_{MW} was dominated by noise (even at reasonable SNR), thus reducing

the applicability for between-subject comparisons of populations. Conversely, f_{MT} had excellent precision as shown from both simulation and experimental results. To generalize these findings, we determined a longitudinal study would require up to 261 participants to detect a 5% change in f_{MW}, while only 18 participants were required for f_{MT}. In summary, the MT method is more reproducible and robust to measurement error than MW, and may be a feasible application for tracking age-related change in myelination.

3.2 Introduction

Magnetic resonance imaging (MRI) is sensitive to myelin, which can be indirectly assessed using myelin water (MW) and magnetization transfer (MT) imaging techniques [97,98]. Myelin is comprised of lipid membranes that are wrapped tightly around axons to form many layers of semi-permeable insulation [25]. MW is sensitive to distinct relaxation characteristics of hydrogen protons of water (WPs) sequestered between individual layers of myelin [54,55]. MT measures the transfer of magnetization between WPs and non-water hydrogen protons such as the proteins and lipids of biomembranes and macromolecules (MPs) [73]. In white matter, myelin layers are the predominate source of MPs, contributing to the prevalent use of MT for myelin imaging. While the physical mechanism of MT is not specific to only myelin layers, several studies have suggested MT imaging techniques to be more precise, and thus more reproducible than MW imaging [59,86,99]. Even so, recent developments in the acquisition and analysis of MW and MT techniques invite reassessment of their relative advantages for assessing myelin content. For this study, we evaluated the performance of two recently developed MW and MT methods [63,100–102].

A primary source of MRI contrast is produced by the apparent relaxation of WPs. While WPs are free to diffuse and interact with their local environment, they experience complex interactions due to insoluble inter- and intracellular components of the cellular milieu. Myelin

membranes restrict WP diffusion to spatially defined compartments. This is useful in MRI, as WP pools adopt different relaxation characteristics based on their microenvironments. For example, WPs trapped between myelin layers exhibit a fast transverse relaxation (T_2 ~ 15 ms at 3 T) relative to intra-/extracellular water pools (T_2 ~ 80 ms at 3 T) [94]. Conventional MW imaging uses a multi-spin echo (MSE) sequence to acquire T_2 decay curves [103]. A non-negative least-squares (NNLS) fitting algorithm is then used to assign myelin and intra-/extracellular water signals as a function of their T_2 distribution. From this, myelin water fraction (f_{MW}) is defined as the fraction of water in the myelin sheath compared to total water, and can be estimated from short T2 signal over total.

The NNLS algorithm is often constrained, or "regularized," to reduce noise in model fitting [104,105]. This improves the reliability of assigning a f_{MW}, but can also lead to misclassification, especially in images with low SNR (<100) or atypical water distributions, such as in edema and inflammation [105]. Alternatively, MGRE imaging has been used for extracting both T_2* relaxation and resonant frequency shifts in white matter. Particular tissue constituents, such as myelin, can induce small, but detectable, field shifts based on their magnetic susceptibilities [106]. Faster dephasing of WPs (i.e., shorter T_2*) and larger frequency shifts have been attributed to increases in both myelin content and anisotropy of myelin sheaths. For this study, we applied a multi-exponential fitting algorithm to the MGRE data to model three compartments: the myelin, axonal, and interstitial signal fractions. A primary benefit of this approach is the additional information for the model arising from the magnetic susceptibilities of myelin. However, these effects are field dependent, meaning the sensitivity of T_2* and frequency shifts will scale with increased magnetic field strength [107]. This caveat was discussed in Chapter 2, and may indicate that this method will also be unreliable for application at 3 T. Even so, this

approach has gained popularity for myelin imaging in clinical populations, and thus must be rigorously evaluated for long-term use.

Myelin membranes also contribute a significant portion of non-water, or "macromolecular" protons (MP), associated with lipids and proteins. MPs are MR-invisible due to ultra-short T_2 relaxation times (outside the capabilities of scanner hardware for human imaging), but can be indirectly assessed using MT experiments [73]. The MT effect is modeled on changes in longitudinal relaxation, or T_1. Conventional T_1 imaging measures the relaxation of WPs, but can be modified by irradiating MPs with specialized radio-frequency (RF) pulses. This irradiation creates a magnetization difference between WP and MP, and over time the process of MT restores this difference to zero. During this equilibration, a transient change in the WP magnetization is observed, also known as the MT effect. The strength (i.e., magnitude) of this MT effect is relative to MP pool size, or f_{MT}, which is the main source of T_1 contrast in lipid-rich white matter [108]. The f_{MT} can then be estimated by fitting a two-pool model of WP and MP exchange to the MT data.

One way to measure MT effects is to apply an "MT pulse" to selectively saturate MPs, then compare signal with the pulse and without the pulse (MT off – MT on / MT off). Conventional MT sequences use a long series of repeated pulses to measure saturation effects in a steady state, (i.e., a constant difference in magnetization between pools) [109]. This technique is very sensitive to MT effects, but also depends on experimental parameters, such as frequency and irradiation power of the MT pulse [110,111]. An alternative and potentially faster way to measure MT is to use a single, strong MT pulse, to observe transient exchange of WP and MP over time [101,102,112]. Apart from being insensitive to RF pulse power and frequency, this technique is efficient in saturating the MP pool (~90%), and only minimally saturating the WP pool

(~10%). For these experiments, the transient MT approach was analyzed using a two-pool model of exchange to quantify f_{MT}.

While both MW and MT techniques provide a relative measure of myelin content, they are not a direct quantification of myelin volume and thus cannot be directly compared. Additionally, each technique is influenced by different contrast mechanisms, experimental conditions, and model precision. Differences can also arise when f_{MW} does not fully describe myelin water, or when f_{MT} includes lipid signal from more than myelin membranes. Even so, it is important to establish the technique that provides the greatest reproducibility and thus would be useful for tracking underlying biological changes in myelin. The goal of this work was to compare the performance of MW and MT imaging techniques described above. We first established putative error levels using repeat measurements across the experimental cohort. From this, we simulated how model fitting performed under the influence of various levels of noise. Model precision of myelin parameters was quantified by comparing simulated versus inter-subject variance for each technique. Finally, we used an *a priori* power analyses to examine the feasibility of detecting small differences in f_{MW} or f_{MT} within the same subjects over time [113] from which we estimated the sample sizes that would be required for a longitudinal study for both techniques.

3.3 Methods

3.3.1 Participants

Healthy adolescents were recruited from the Washington, DC, Maryland, and Virginia areas for participation in a five-year longitudinal project on adolescent brain development [114]. Study procedures were approved by the Georgetown University Institutional Review Board, and all youth and legal guardians provided informed assent and consent, respectively. The study

included MRI testing and cognitive assessment over three visits, spaced ~ 18 months apart. Criteria for exclusion were known psychiatric conditions, cognitive impairment, parent-reported prenatal alcohol exposure, prior drug or alcohol use, and left-handedness. Additional detail on baseline recruitment procedures and exclusion criteria are reviewed extensively in [114]. Data were acquired on 106 subjects collected for this study, and 13 were excluded due to severe motion artifact or incomplete data during data acquisition. The following analyses includes 93 participants, ages 12.7 – 16.8 (see Table 3.1), who completed an MRI scan during their second study visit (out of three total visits).

Table 3.1 Participant demographics. Sample size and average age ± SD are reported for total scans (MGRE and/or EPI), MGRE scans only, and EPI scans only. There was a large overlap (48 scans) between datasets; thus, no significant differences were observed in age.

Demographics			
Sequence	Total	MGRE	EPI
N	93	61	80
Age	14.4 ± 0.8	14.5 ± 0.8	14.3 ± 0.8

3.3.2 Data acquisition

General scanning protocol

For the MW approach, signal amplitude and phase evolution were acquired with a multi-gradient echo (MGRE) pulse sequence, and analyzed by fitting a multi-exponential model to these data. Compartment-specific T_2* and resonant frequency shifts were used to describe myelin, axonal and interstitial water pools. Myelin was estimated as the fraction of myelin water signal amplitude (f_{MW}) to total water sources. For the MT approach, we acquired two sets of echo planar imaging (EPI) scans using 1) a transient, double inversion pre-pulse (MT pulse) to

estimate MT effects, and 2) a single inversion pre-pulse (IR pulse) to establish T_1 relaxation. MT and IR scans were co-jointly analyzed using a two-pool model to extract a macromolecular proton fraction (f_{MT}), an indirect measure of myelin. MGRE and EPI scans were collected on a 3 T scanner (Siemens, Erlangen, Germany; Tim Trio platform) using a 12-channel receive only coil. Multiple repetitions of each scan type were acquired during a single scanning session. For example, the MGRE sequence was repeated three times in one session; then, the MT-labeled EPI sequence was repeated fifteen times in one session. The MGRE sequence took longer to acquire, and thus there were fewer total repetitions. These repetitions, i.e. "repeat measurements," were used to calculate the within-scan stability for each sequence. For between subject comparisons, scan repetitions were averaged prior to parameter estimation to improve the signal-to-noise ratio of the data. MGRE scans were positioned in axial orientation, co-planar with the anterior commissure and posterior commissure (AC-PC) to cover the corpus callosum. All scans were aligned to the center MGRE slice during acquisition to ensure the same tissue coverage. The five-slice EPI scans were spaced to allow direct overlap with every third slice of the MGRE scan.

Myelin water imaging

The MGRE sequence was acquired using similar parameters as described in Chapter 2 (Methods). Image processing and model fitting were done in the same way, and will only be briefly mentioned below.

Scanning protocol

MGRE data were acquired using the following parameters: 240x180 mm^2 FOV, 160 x 120 resolution, fifteen 1.5 mm slices (25% gap), SENSE rate 2, 1275 ms repetition time (TR), and a bandwidth of 250 kHz. There were 41 positive-only echoes with echo time (TE) = 2.86-80.60 ms and an echo spacing of 1.92 ms. Each image set had three repetitions; resulting in scan time of 6 min. The phase of each image set was filtered using a linear offset over TE and for each slice.

Parameter estimation

MGRE signal in white matter is sensitive to distinct relaxation and frequency offsets of myelin, axonal, and interstitial water components. We can model these effects to estimate the relative myelin fraction in white matter using the following multi-exponential equation:

$$S = (A_1 e^{(-R^*_{2,1}+i2\pi\Delta f_1)t} + A_2 e^{(-R^*_{2,2}+i2\pi\Delta f_2)t} + A_3 e^{-R^*_{2,3}t}) e^{i(2\pi f_g t+\varphi)} \quad [1]$$

A three-component model was fit to complex signal (S) where i was the imaginary unit, A_n the amplitude, $R^*_{2,n}$ the relaxation rate, Δf_n the frequency shift calculated as relative to a global/interstitial frequency, f_g, and φ the phase offset. Components 1, 2, and 3 correspond to myelin, axonal, and interstitial water, respectively. The f_{MW} is the fraction of $A_1/(A_1 + A_2 + A_3)$.

Magnetization transfer imaging

Recent technical developments have enabled the efficient mapping of an MP fraction (f_{MT}) in brain tissue using a transient MT pulse design [101,102,112]. Using this method, we extracted the f_{MT}

and other model parameters (k_{wm}, k_{mw}, R_{1w}) based on fitting a bi-exponential, or two-pool model, to saturation (MT) and inversion recovery (IR) longitudinal relaxation curves.

Scanning protocol

MT scans used a dual hyperbolic-secant inversion RF pulse ("MT pulse") to selectively saturate the MP fraction. Following a variable delay time, signal was measured with an EPI sequence with: 240x180 mm^2 FOV, 144x108 resolution, five 2 mm slices (181% gap), SENSE rate 2 (with external gradient echo based reference), 2 s TR, 30 ms TE, and a bandwidth of 250 kHz. Delays of 10, 71, 132, 193, and 254 ms with a duration of 6 ms were used for the MT pulse. MT pulse amplitude (B_1) was set to 750 Hz, or close to maximum for this scanner. These parameters were previously determined to saturate the MP pool up to ~90%. On the first cycle, a different slice was imaged at each of the five delay times. Then on each following cycle, the slice order was shifted +1 slice such that each slice was acquired with the next increment in delay time. By shifting slices in this way, all five slices were cycled through a complete set of five delay times (Figure 3.1) [102].

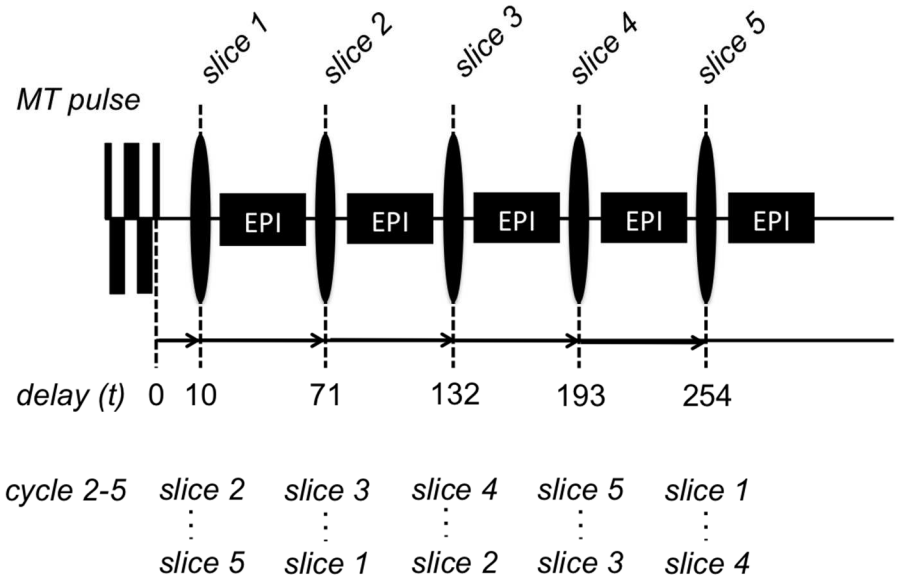

Figure 3.1 Slice sampling and time delays of the magnetization transfer pulse sequence. Delay times listed are for MT scans. For this scheme to work, the slice count must be some multiple of the total delay times (for example, 5 slices = 5 inversion times; or, 15 slices = 5 inversion times). Only five slices were acquired, as wide slice spacing is useful for minimizing latent saturation effects between slices. Adapted from [102].

The five scan cycles used to sample all slices at all delays constituted one scan repetition. Scan time was 6:16 min for a total of eighteen repetitions, where three were acquired with no MT pulse to serve as reference scans.

For IR scans, the MT pulse was replaced with a single hyperbolic-secant inversion pulse. Delay times were set to 9, 203, 461, 843, and 1600 ms, with a pulse duration of 5.12 ms and B_1 amplitude of 750 Hz. IR scans used a TR of 3 s, and acquired only four repetitions (two for reference signal), taking a total scan time of 1:24 min. Slice positioning was matched to MT scans.

Parameter estimation

A two-pool model of exchange was fit to both MT and IR experimental data. This allowed for the estimation of the MP pool fraction, f_{MP}.

$$S_{WP}(t) = 1 - \frac{M_{WP}(t)}{M_{WP}(0)} = a_1 e^{-\lambda_1 t} + a_2 e^{-\lambda_2 t} \quad [2]$$

$$2\lambda_{1,2} = \left(R_{1,WP} + R_{1,MP} + k_{MW} + k_{WM} \pm \sqrt{(R_{1,MP} - R_{1,WP} + k_{MW} - k_{WM})^2 + 4k_{MW}k_{WM}} \right) / 2 \quad [3]$$

$$a_{1,2} = \pm \frac{S_{WP}(0)(R_{1,WP} + k_{WM} - \lambda_{2,1}) - S_{MP}(0)k_{WM}}{\lambda_1 - \lambda_2} \quad [4]$$

$$(1 - f_{MT})k_{WM} = f_{MT}k_{MW} \quad [5]$$

Here, $M(t)$ is the longitudinal magnetization, which is converted to the fractional saturation, *S*. The λ_1 and λ_2 are fast and slow rate constants, respectively, and are determined by the relaxation (R_1) and exchange rates (k_{WM} and k_{MW}) of the tissue. The amplitudes (a_1 and a_2) depend in part on the effectiveness of the MT pulse in saturating the MP pool. To calculate these parameters, one pair of rate constants (λ_1 and λ_2) and two pairs of amplitudes (a_1 and a_2) were extracted by jointly fitting the MT and IR data with Eq. [2]. The remainder of the analysis required solving for six unknowns: $S_{WP}(0)$, $S_{MP}(0)$, $R_{1,MP}$, $R_{1,WP}$, k_{WM}, and k_{MW}. The $S_{MP}(0)$ and $R_{1,MP}$ cannot be directly measured (MR-invisible pool), but were estimated in previous *in vivo* experiments and simulations in white matter [101]. Using these values, we fixed $S_{MP}(0)$ to 0.88 (1.0 being the maximum saturation), and $R_{1,MP}$ to 4 Hz for this study. We then used the decay rates and amplitudes from Eq. [2], and the fixed parameters ($S_{MP}(0)$ and $R_{1,MP}$) to calculate the $R_{1,WP}$, exchange rates, and ultimately, f_{MT}.

3.3.3 Data processing

All datasets were aligned using in-plane registration. White matter ROIs were drawn on MGRE images, including bilateral optic radiation (OR), splenium (SCC) and genu (GCC) of the corpus callosum, and a bilateral mid-frontal white matter region (FLWM). ROI masks were then down-sampled and applied to EPI datasets. ROI positioning was rechecked for each EPI scan type, and edited if necessary to avoid artifacts from motion or susceptibility distortion. Scan repetitions with unusable data were excluded from both the reproducibility and between subject comparison analyses. Each repetition was evaluated as a stand-alone repeat measurement to test the stability of each method. To compare between subjects, repetitions were averaged for each scan type to maximize available image SNR. All image reconstruction and processing was done in IDL version 8.6 (Exelis Visual Information Solutions, Boulder, CO, USA).

3.3.4 Statistical analyses

Simulations were performed in IDL and statistical analyses were done in R version 3.3.1.

Stability of repeat measurements in MRI data

To test the reproducibility of each technique, the within-scan variance was pooled across all scan repetitions for all subjects. The pooled standard deviation (SD_p) was defined as measurement error, where high SD_p (high error) indicated a poor level of reproducibility. Each repeat measure comprised the average signal across all voxels within an ROI. This approach resulted in region specific error levels, allowing us to make inferences on the stability of subsequent parameter estimations [115,116]. Of note, this error term is sensitive to several contributions, such as random machine noise and subject motion [117]. While machine noise has a normal distribution in MRI

data, subject motion may amplify variability across repetitions. Even so, precautions were taken by excluding entire repetitions and individual ROIs when artifact was present.

The SD_p takes the average spread of data points about each set of repeat measurements, then calculates a weighted average of the within scan variability. This equates to a single estimate of the common variance across all subjects. This is useful for when signal means differ (but variance is roughly the same), or if there are different numbers of repeat measurements for each subject. Thus, each repeat measurement is equally weighted regardless of the total number of repeat measurements for a particular subject. The SD_p was calculated for MGRE and MT scans separately, as each scan type uses a different sequence and acquisition parameters. The formula for SD_p is shown in Eq. 6:

$$SD_p = \sqrt{\frac{\sum_i \sum_j \left(x_{ij} - \bar{x_i}\right)^2}{\sum_i (n_i - 1)}} \quad [6]$$

The average signal, $\bar{x_i}$, for all measurements is subtracted from each individual measurement, x_{ij}, taken during one scanning session. Next, the sum of squares is taken for each measurement (*j*) across all subjects (*i*). This result is divided by degrees of freedom (*df*), i.e., the sum of all repeat measurements minus the number of subjects. The SD_p is the square root of the final result.

For MGRE data, the SD_p was calculated for the complex input signal (*S*) in Eq. 1. Signal magnitude was normalized ($S_{TE(0)} = 1$) and SD_p reported as the percent absolute signal. Absolute SD_p of phase was reported in radians. MGRE scans with only one artifact-free repetition were excluded prior to this study, leaving two or three repetitions for this analysis. For the MT dataset, error was estimated for the input signal in Eq. 1, or $S_{WP}(t)$. The $S_{WP}(t)$ was calculated by

dividing pulsed, or "labeled" MT scans ($M_{WP}(t)$), by the unlabeled reference scans ($M_{WP}(0)$). For each delay time, SD_p was calculated using fifteen labeled scan repetitions. The SD_p was then calculated separately for the fifteen reference scan repetitions. A composite SD_p for the input signal was calculated using a propagation-of-error analysis [118]. This calculation produces a relative SD_p, and is reported as a percentage. The SD_p is not only useful for examining the repeatability of each technique, but also sets an expectation for baseline noise levels prior to model fitting.

Descriptive statistics of experimental results

Descriptive statistics were computed for each technique in each ROI to assess model-fitting performance. In particular, mean and standard deviations are reported for each estimated myelin-sensitive parameter (f_{MW},f_{MT}). Additional model parameters are reported in Supplementary Table 3.S1 and were used as data for the simulations.

Simulations: Influence of noise on parameter estimation

Simulations were performed to study the precision of model fitting under the influence of noise. Noise levels were selected from the SD_p of experimental data, which were 0.5% for MGRE and 1.0% for MT. For MGRE, synthetic decay curves were simulated using Eq. 1 and ROI-averaged experimental parameters (Table 3.S1, A). To replicate MGRE pre-processing steps, three signals with noise were averaged for each trial of model fitting. For MT, saturation recovery signals were generated using Eq. 2 and ROI-averaged parameters (Table 3.S1, B). Fifteen signals with noise were averaged prior to model fitting. Model fitting was performed for 1,000 trials of each signal type, and SD was calculated for fitted myelin parameters.

Sample sizes from a priori power analyses

Sample sizes required to detect a difference in myelin parameters were calculated for a paired sample design (i.e., simulating subjects scanned at two time points). Average SCC results (mean, SD) were used as Time 1 data (Table 3.2). For Time 2, mean was increased by 5% and SD was set to the same relative variance as Time 1. The effect size was calculated as the standardized mean difference between time points. Sample size was then estimated for a two-sided, paired sample t-test at a significance of $\alpha = 0.05$ and power level of 95% (1- β).[119–121].

3.4 Results

Stability of repeat measurements in MRI data

Error levels were similar between both MGRE and MT scans. The SD_p for MGRE magnitude was ~0.5% of total signal at early echo times, and increased up to 1% for later echoes (Figure 3.2, A). Later echo times are progressively more susceptible to field inhomogeneities, which would account for the increase in SD_p. The SD_p of MT input signal was consistent for each delay time, ranging from ~1% to 1.6% (Figure 3.2, C). Anterior brain regions, such as GCC and FLWM had higher percent error for both MW and MT since they were impacted by susceptibility artifacts arising from proximity to the sinus cavities.

The SD_p of MGRE phase data are reported in absolute values of radians (Figure 3.2, B). A phase of ~ 0 is considered "on-resonance," as it is dominated by the mean resonance frequency of tissue water. Deviations in phase are due to disruptions in the local magnetic field. This is in part due to random error, but there are also systematic shifts in magnetic susceptibilities from tissue microstructure.

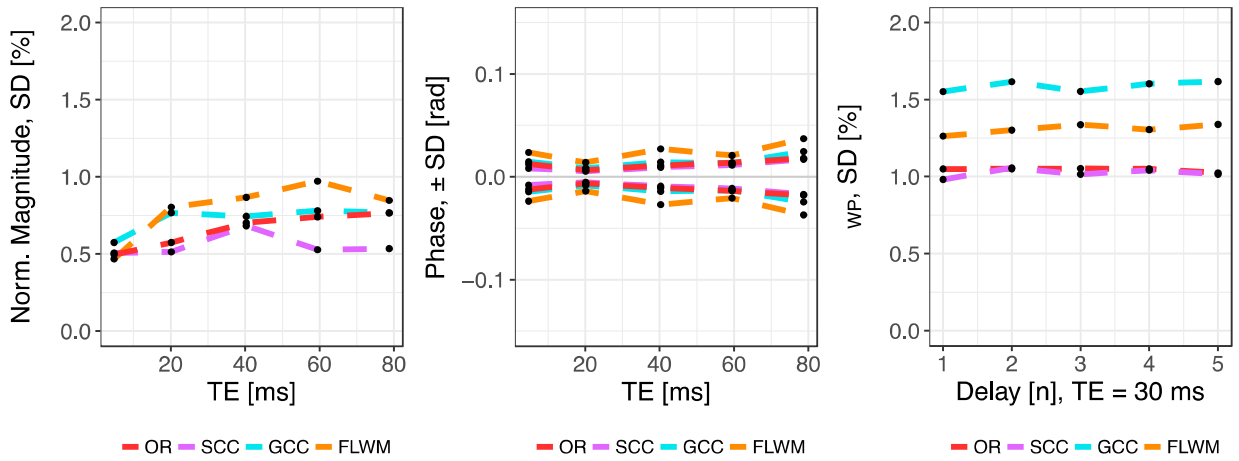

Figure 3.2 Within-scan variance for MGRE and MT data. SD_p was calculated across repeat measures for each subject. A, B) Five TEs were sampled at regular intervals across the total MGRE echo train. MGRE magnitude signals were normalized ($S_{TE(0)} = 1$) and reported as percent signal. C) Relative SD_p is shown for MT for five delay times.

Descriptive statistics of experimental results

Descriptive statistics were examined for each fitting routine (Table 3.2). The MW method had high variance for f_{MW}, with a two- to threefold increase in anterior brain regions relative to the posterior ROIs. This is primarily due to the proximity of susceptibility artifacts, which corrupts the estimation of local frequency shifts for each water compartment. The MT model had lower inter-subject variability for each ROI than the MGRE method (~6%). All standard deviations are also reported as a percentage of the mean to compare the variance between methods.

Table 3.2 Descriptive statistics of myelin parameters. Average and SD of fitted parameters for all subjects. Data were excluded from individual ROIs due to localized artifact. The absolute mean and SD of f_{MT} and f_{MW} do not directly measure myelin content and cannot be compared. A relative SD (%) was calculated as the ratio of SD to the mean as a percentage.

Par	ROI	N	Mean	SD	SD (%)
f_{MW}	OR	59	0.146	0.027	18.49
	SCC	61	0.124	0.027	21.77
	GCC	61	0.091	0.041	45.05
	FLWM	59	0.109	0.067	61.47
f_{MT}	OR	72	0.246	0.015	6.10
	SCC	80	0.256	0.014	5.47
	GCC	72	0.266	0.018	6.77
	FLWM	74	0.240	0.014	5.83

Simulations: Influence of noise on parameter estimation

As shown in Chapter 2, model fitting of MGRE data when little or no noise is present does not result in an accurate estimate of A_1 (Figure 2.4 in Chapter 2). This was most obvious in the 0% noise condition (before additive noise masked the effect). Of note, Chapter 2 used a substantially lower noise than we found in the experiments above (~ 0.1% at 3 T). This low value originates from a pre-scan measurement to specifically sample random signal fluctuations in air, i.e., pure, random noise. The current metric was sampled to reflect both pure noise *and* within scan variance. While this technique results in larger variability, it is a better reflection of average noise present for all subjects.

The standard deviations (SD_{ERR}) from noise simulations are presented in Table 3.3. Because the parameters are not on the same scale, the relative SD_{ERR} (%) was calculated as the percentage of SD_{ERR} to input value. These results show f_{MW} had at least two times higher relative variance (i.e., SD_{ERR} (%)) than f_{MT}. Variance also increased relative to increased noise levels (data not shown). The MT method was more accurate in solving for expected f_{MT} with the

relatively low SD_{ERR} (%) (~ 3-5% with 1% added noise). Figure 3.3 shows the distributions of f_{MW} and f_{MT} across all subjects.

Table 3.3 Variance in myelin parameters due to noise. Absolute and relative SD_{ERR} of model parameters over 1,000 trials of simulated data at σ = 1.0%. Relative SD_{ERR}(%) is the ratio of SD_{ERR} to input value as a percentage.

Par	σ	ROI	Input	SD_{ERR}	SD_{ERR} (%)
f_{MW}	0.5%	OR	0.146	0.016	11.2
		SCC	0.124	0.021	16.9
		GCC	0.091	0.011	12.1
		FLWM	0.109	0.027	24.5
f_{MT}	1.0%	OR	0.246	0.0119	4.8
		SCC	0.256	0.0093	3.6
		GCC	0.266	0.0086	3.2
		FLWM	0.240	0.0087	3.6

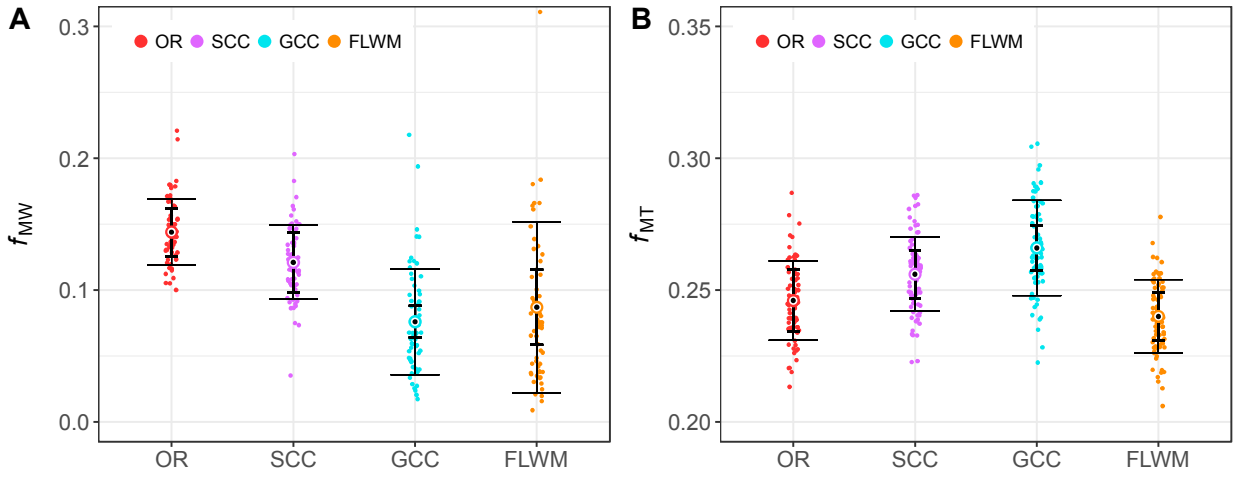

Figure 3.3 Distribution of ROI-based fitting results for each method. Scatterplot of fitted model parameters for all subjects by ROI. The outer error bars are the SD for all subjects (Table 3.2); the inner error bars SD_{ERR} are from the noise simulations (Table 3.3). The absolute values of f_{MT} and f_{MW} do not directly measure myelin content and cannot be compared. The y-axis as been rescaled in panel B to highlight small differences in f_{MT}.

Sample sizes from a priori power analyses

Sample sizes required to detect a 5% change were calculated using the above data to estimate the effect sizes and standard deviations assuming 95% power and a significance level of $\alpha = 0.05$. The required number of participants was 261 for MW and only 18 for MT. These values reflect one-sample paired t-test, and do not include adjustments for multiple comparisons if multiple ROIs were tested. Thus, if more tests were conducted, the sample size would naturally need to be increased relative to number of ROIs considered. MW required much larger sample sizes relative to MT and is thus impractical for detecting small effects.

3.5 Discussion

This study examined the precision of myelin parameter estimation using MT and MW techniques. *In vivo* MW imaging had remarkably high parameter variance across participants, with relative SD (%) for f_{MW} being three to ten times greater than for f_{MT}. The stability of repeat signal measurements was comparable between datasets, implicating model performance as the source of large differences in *in vivo* parameter variance. Data simulations showed that MW model fitting was indeed highly susceptible to even small differences in measurement error, and an unreliable estimator of f_{MW}.

While the focus of these analyses has been on myelin content, each parameter is important for describing specific attributes of signal evolution. Model parameters are highly interdependent on each other, and error and/or bias in any individual parameter can adversely influence estimation of myelin content [122]. For MW, ten parameters are fit to the MGRE signal using three compartment-specific decay functions. From Chapter 2, we know that a variety of parameter values, especially for axonal and interstitial compartments, can be used to fit the same MGRE data with limited or no penalty. The lack of sensitivity for extracting precise estimates of

these values implies the parameter of interest, in this case, f_{MW}, will be unreliable, which corresponds to the high variance observed in these data. Conversely, noise simulations for f_{MT} varied by only 3-5% for each tissue region at 1% added noise relative to the total signal (equivalent to SNR = 100). This reduction in variability is due in large part to the fact that the MT method fits only six parameters using a two-pool model of exchange. Further, these, two parameters, $S_{MP}(0)$ and $R_{1,MP}$, are constrained to pre-defined values for all brain regions [102]. Assigning fixed values to parameters improves precision by simplifying the model, but also imparts biases and decreases accuracy of other derived parameters. For example, previous MT studies had estimated $R_{1,MP}$ to be approximately 1 s^{-1} at 1.5 T [80]. Using a similar imaging protocol as presented in this study, van Gelderen et al. estimated $R_{1,MP}$ to be much higher at ~ 4 s^{-1} for 3 T, and demonstrated that low $R_{1,MP}$ leads to a significant underestimation of f_{MT} [102]. The $R_{1,MP}$ parameter is difficult to estimate empirically, and may vary across tissue types, such as in regions with high iron, or in white matter pathology with atypical MP/WP distribution. As such, we must be cautious in interpreting f_{MT} as a direct index of myelin, although it is far more reproducible than f_{MW}.

The interdependence of model parameters is complex, and difficult to establish for multi-compartment models. Propagation of error analyses and variance estimates can be useful tools for uncovering model limitations, which might not be easily discerned from *in vivo* human subject data. For example, a simulation study examined the lowest possible parameter variance for an alternate myelin model, called mcDESPOT [122,123]. The McDESPOT method fits a two-compartment model to both T_1 and T_2 signals to extract a myelin parameter that is similar to f_{MW}. The simulation study predicted extremely high parameter variance for f_{MW}, that exceeded variance observed from *in vivo* studies. The authors suggested this model oversimplified certain

physical properties in white matter, and received an artificial boost in precision due to this "inherent parameter constraint." As previously discussed, fixed parameters, whether inherent or explicitly defined, can lead to systematic errors, even in cases where the average across multiple subjects looks reasonable. In light of this, we compared the variance due to measurement error versus the variance of between subject results (Figure 3.3). If SD_{ERR} were equal to or greater than subject SD, it would indicate that measurement error had completely dominated the average variance, and would be insensitive to subject-specific effects. We did not observe this; however, it should be noted that the repeat measurement error used as the basis of noise simulations were selected as "best case scenarios" for each set of input signals. Because the measurement error was calculated over ROIs, it is unlikely these effects will be due to random machine noise, but be driven by a variety of scan-to-scan effects, such as subject motion and regional instabilities. The best-case scenario resulted in error levels most similar to SCC and OR, at ~ 0.5% for MW and ~ 1% for MT. Therefore, the large discrepancies observed between SD_{ERR} to SD for anterior ROIs may underestimate the absolute difference in variance for these regions. This is especially true for MW, as this model is particularly sensitive to any measurement instabilities. We also tested "worst case scenarios" (data not shown), which were similar to GCC and FLWM, at ~ 1% for MW and ~ 1.5% for MT. In this instance, SD_{ERR} did exceed SD for SCC and OR in the MW results only. This scenario indicates that even a small change in error at the individual subject level would propagate to the in inaccurate estimation of f_{MW}.

Previous comparisons of multiple spin echo (MSE)-MW and MT parameter estimates of myelin have reported similar ratios of variance between subjects. In a clinical study, MT parameters were sensitive to lesion recovery, while MSE-MW imaging was unable to detect any change due to high variability [59]. Investigators concluded the twofold increase in variance of f_{MW}

was due to the ill-posed nature of the multi-exponential analysis. As with our MGRE data, MSE imaging acquires a limited number of data points (based on echo times) with which to fit the parameters of the model. Limited data leads to poor precision, which can mask subtle biological effects. Even so, many studies have shown MSE-MW and MT imaging methods to provide correlative measures of myelin content [57,58,98,124]. A recent study went beyond correlation, and compared the accuracy of MSE-MW and MT parameter estimates to a histological measure of myelin volume fraction in mouse brain [56]. While both parameters had high correlations to histology (r = 0.81, 0.84 respectively), neither provided the complete myelin volume fraction. The MSE-MW parameter underestimated myelin volume across all tissue samples, which may be partially due to inter-compartmental water exchange in areas of thin myelin sheaths and small axons [57,98]. The MT parameter both overestimated low myelin volume, and slightly underestimated high myelin volume. This may be due to the oversimplification of complex biophysical effects, such as the presence of additional non-water pools. In general, however, the rank order of low to high myelin volume fractions, irrespective of differences in microstructure, was preserved for each method. For this study, the expected rank order of OR, SCC, GCC, and FLWM were roughly inverted between techniques (Figure 3.3). The f_{MW} had high variance and unexpectedly low values for GCC and FLWM, while f_{MT} had similar variance across all tissue regions. Based on the sensitivity of MW to noise, the f_{MW} results are most likely dominated by error versus inter-subject variability.

Our goal in this study was to determine whether these techniques could be used to measure longitudinal change throughout adolescent development. However, the sample size needed to detect a significant effect may limit its usefulness for research and clinical applications at least in the case of MW. Based on previous imaging studies, we predicted only ~5% increase

in myelin parameters for adolescents in this age range [35]. Sample size was calculated based on the magnitude of our hypothesized effect, variability between subjects, and preset statistical thresholds (alpha = 0.05). For a 95% power level, we would need 261 subjects for the MW approach, which would still suffer from unreliable estimates in regions of high measurement error (e.g., anterior ROIs). For MT, only 18 subjects were required for a paired t-test. *In vivo* studies are often limited to small effects, and the selection of MT would be merited for this type of application.

A potential limitation of this study was including only repeat measurements from within the same scanning session. An alternate approach would be to scan the same subject(s) across a series of days. This design of the current study did not include short-term repeat measurements (over days), and longer scan deltas (~1.5 yrs) would be to large given the potential introduction of age-related effects in adolescents. Even so, we used a large sample for these analyses, and could reasonably infer differences in model stability for each technique. The current project was part of a larger developmental study, and limited to a fixed scan time of 20 minutes. This is not uncommon in neuroimaging studies, especially when collecting data that is complementary to a primary goal (functional imaging in this case). However, if time allows, and patient comfort is not sacrificed additional scan repetitions could be acquired for small improvements in measurement stability.

3.5.1 Conclusions

We compared the precision of MW and MT imaging techniques in a sample of healthy adolescents. The MW multi-exponential model was highly susceptible to measurement error, and produced f_{MW} values with much higher variability in anterior tissue regions. In contrast, the MT

technique was very robust and had high precision for all regions sampled. Furthermore, the estimated sample sizes required to detect even a 5% change were over 14 times higher for MW than MT. Thus, the MT technique would be suitable for longitudinal studies of adolescent development and most likely other studies attempting to measure changes in myelin.

Chapter IV. Regional age-related changes in relative myelin content during adolescent development

4.1 Overview

The spatiotemporal growth trajectories of white matter, and in particular myelin, are an important part of cognitive development during adolescence. Cross-sectional and longitudinal studies have demonstrated age-related white matter changes using various MRI techniques, with association areas and tracts continuing to mature well into adulthood. Magnetization transfer imaging techniques have shown increased sensitivity to myelin content versus standard techniques, with the potential for detecting small, age-related changes. The goal of this study was two-fold: 1) test whether a novel MRI technique for estimating myelin content could detect developmental changes over a relatively short time span and 2) determine the extent to which these changes in myelin are associated with change in executive function. For this study, we tested 56 adolescents at two time points spaced 18 month apart. A newly developed magnetization transfer (MT) imaging technique was used to estimate the relative myelin content, f_{MT}, in four white matter regions. Regions were selected across an early to late myelinating developmental continuum, including the optic radiation, splenium of corpus callosum, genu of corpus callosum, and frontal lobe, respectively. Executive function was assessed using two well-validated measures: Trail Making Test B and the Spatial Working Memory test from CANTAB. We found f_{MT} in frontal lobe white matter significantly increased ($t_{(49)} = 3.19$, $p = 0.003$) with a small to moderate effect size (Hedges's $g = 0.36$). There were no associations of age-related change in regional f_{MT} with either test of executive function. Our inability to associate changes in

executive function with myelin changes may in part have resulted from the relatively narrow range of ages studied.

4.2 Introduction

The adolescent brain undergoes significant changes to "fine-tune" neural substrates prior to adulthood [34]. Histological studies have implicated white matter, and more specifically the myelination of axons, as an important biological process in brain maturation [25,33,125]. Myelin facilitates the enhanced speed and synchrony of electrical transmission between brain regions, and provides trophic support for neurons throughout the central nervous system [126]. The process of myelination follows a stereotyped developmental pattern, which mirrors the functional capacity of neural systems [31]. For example, myelination of primary sensory and motor regions typically mature by the first two years of life, whereas frontal and temporal association regions do not peak until well into adulthood [32,127]. *In vivo* MRI studies have played a major role in elucidating white matter changes of individual brain regions and connecting pathways, and relating these changes to cognitive maturation. In adolescence, increases in white matter have been associated with metrics such as working memory, inhibitory control, processing speed, and reading ability [128–131]. Even so, it is still unclear how the timing and/or change in magnitude of individual myelin content might relate to developmental changes in cognition during adolescence.

MRI studies of white matter development have typically used either volume-based segmentation of T_1-weighted contrast or standard diffusion tensor imaging (DTI) techniques [132–134]. High-resolution imaging has improved volume estimates, but it is limited by a lack of specificity to biological features (myelin, axon caliber, vasculature, head size, etc), resulting in poor sensitivity to more subtle developmental effects [135,136]. DTI parameters, such as fractional

anisotropy (FA), are more sensitive to myelin than white matter volumetric measures, and have been used to show non-linear trajectories of the development of white matter tracts across children, adolescents, and adults [35,52,137]. White matter tracts are comprised of densely packed, myelinated axons, which restrict water diffusion along the length of the axon. FA is sensitive to the dispersion of water within a voxel, and has shown good correspondence to myelination, fiber density and organization [138,139]. However, this technique is limited to a statistical description of water diffusion, and cannot directly infer myelin content [52]. A number of more specialized DTI techniques have been recently developed to detect specific microstructural characteristics and resolve past limitations [140–142]. While promising, these techniques require nonstandard image acquisition (longer scan times) and processing, and have not yet been incorporated into large-scale adolescent studies due to these limitations [143]. Thus, standard volume and DTI techniques have been difficult to interpret from a biological perspective of myelin maturation.

Alternatively, magnetization transfer (MT) imaging techniques have been used to investigate changes in myelin content. MT contrast reflects the exchange of magnetization between free water protons (WP) and protons bound to macromolecules (MP) [73]. MPs are abundant in myelin membranes; therefore, an increase in MP pool size would indicate more myelin per unit volume (and vice versa for decreases). MT effects can be described using a two-pool model of exchange to extract an absolute measure of MP pool size (i.e., f_{MT}). Several histological studies have suggested f_{MT} is a putative marker of myelin content, even in the presence of diverse microstructural features, such as axonal caliber and myelin thickness [98,124,144]. In addition, increases in f_{MT} has been linked to increased expression of myelin basic protein (MBP) in myelinated cortex of adolescents [145]. MT imaging techniques appear to be sensitive to

myelin content (over standard techniques); however, it should be noted that MT effects are inherently sensitive to all MPs in tissue and do not provide absolute specificity to myelin [146].

For the current study, we applied a recently developed MT sequence to investigate f_{MT} in a longitudinal cohort of adolescents [101,102]. Typical MT experiments apply a series of pulses to saturate the MP pool; then, measure the WP pool at a fixed, or steady-state level of magnetization. The MT-based contrast is then compared to an unsaturated (no pulse) version of the experiment to measure the MT effect. Steady-state can be difficult to achieve in practice, and is dependent on many experimental parameters for estimation of the MP pool size. In contrast, the current technique transiently saturates MPs – then tracks the change in magnetization as a function of pulse delay time (versus the static difference between pools). This approach takes less time to acquire than the steady-state technique, and also provides information about the transient changes in MT saturation.

We used a standard two-pool exchange model to fit MT saturation curves, and extracted the f_{MT} for four white matter regions. Regions were selected to span a continuum of maturation (most to least), including the optic radiation, splenium of corpus callosum, genu of corpus callosum, and frontal lobe [32]. We hypothesized that given the sensitivity of this approach it would be possible to measure developmental changes in myelin over an 18 month period in a group of adolescents. In particular, we predicted there would be a small increase in f_{MT} of genu, which is the main conduit of inter-hemispheric prefrontal connections, and also frontal lobe, which sub-serves frontal and pre-frontal association areas. The development of prefrontal and frontal regions is a hallmark of adolescent executive function processes. As such, we also hypothesized that age-related change in f_{MT} of genu and frontal lobe would predict change in executive function measures that are known to improve during this age-range. Increased f_{MT} in

these regions would support the theory that the fine-tuning of myelin is important for developmentally mediated functions during the dynamic period of adolescence.

4.3 Methods

4.3.1 Participants

Adolescent participants were recruited from the Washington, DC, Maryland, and Virginia areas for participation in a 5-year longitudinal project on adolescent brain development [114]. The study included MRI and cognitive assessments over three visits, spaced ~18 months apart. Participants were ages 11-13 at baseline, and had no history of neurologic or severe psychological issues, cognitive impairment, parent-reported prenatal alcohol exposure, prior drug or alcohol use, or left-handedness. Additional detail on recruitment procedures and exclusion criteria are reviewed in [114]. Study procedures were approved by the Georgetown University Institutional Review Board, and all youth and legal guardians provided informed assent and consent, respectively.

The current study includes 56 participants that completed MRI scans during the second and third study visits (ages 13-15, and 14-17, respectively). This corresponds with the period of time at which the MT imaging sequences were added to the parent study. For simplicity, the labels “Time 1” and “Time 2” will be used to describe the two visits used in the analyses presented herein. Demographic and physical characteristics are presented in Table 4.1. Composite intelligence (IQ) was measured using the Kaufman Brief Intelligence Test (KBIT) [147]. Socioeconomic Status (SES) was calculated by converting the family’s household income to z-scores, averaging both parent’s years of education and converting the average to a z-score, and lastly averaging the income and education z-scores for the final SES measure [148]. Physical stature was measured using Body Mass Index (BMI), which is weight divided by the square of height (kg/m^2) [149,150]. BMI changes rapidly during this time, and females are typically larger than males

in early to mid-adolescence. Therefore, we also report BMI percentiles adjusted for age and sex. This index can be used to classify individuals as underweight (< 5th percentile), healthy weight (≥ 5th and < 85th percentile), overweight (≥ 85th and < 95th percentile) and obese (≥ 95th percentile). Finally, sexual maturity was assessed using the Pubertal Development Scale (PDS) [151]. The PDS includes questions on growth in height, growth of body hair, and skin changes. In addition, boys are asked about the deepening of their voice and growth of facial hair, while girls are asked about breast development and menstruation. Points are assigned based on if a physical change has not yet started (1 point), barely started (2 points), definitely started (3 points), or seems complete (4 points). The average across all questions was calculated and reported in Table 4.1.

Table 4.1 Participant demographics and physical characteristics. Values are reported as mean ± SD for all participants. IQ and SES were assessed at the baseline study visit. Age, BMI, and pubertal status are reported for each study visit. Significance was set to an uncorrected threshold of p<0.05 using a paired, two-tailed *t*-test. Degrees of freedom (*df* = N-1) are reported for each *t*-statistic.

N (pairs)	56			
Sex, F/M	29/27			
IQ	112.76 ± 13.36			
SES	0.14 ± 0.89			
	Time 1	Time 2	*t (df)*	*p*
Age, years	14.31 ± 0.72	15.86 ± 0.73	50.85 (55)	<0.000
BMI, kg/m2	21.59 ± 4.41	22.61 ± 4.77	4.49 (54)	<0.000
BMI, %	59.83 ± 29.38	61.4 ± 27.58	0.94 (54)	*n.s.*
Pubertal Status	2.79 ± 0.55	3.23 ± 0.49	7.41 (51)	<0.000

4.3.2 MRI acquisition

The MT scanning protocol was discussed in Chapter 3 (MRI acquisition). Briefly, MRI scans for both study visits were acquired on a 3 T scanner (Siemens, Erlangen, Germany; Tim Trio

platform) using a 12-channel receive array coil. We acquired two sets of echo planar imaging (EPI) scans using 1) a transient, double inversion pre-pulse (MT) to saturate the MP pool, and 2) a single inversion pre-pulse (IR) to establish T_1 relaxation. The MT pulse was applied at five variable delay times (t = 10, 71, 132, 193, and 254 ms), a pulse duration of 6 ms, and pulse amplitude (B_1) of 750 Hz. Scan time was 6:16 min for a total of eighteen repetitions. Three repetitions were acquired without MT pulse to serve as reference scans. The IR pulse was applied at five delay times (t=9, 203, 461, 843, and 1600 ms), a pulse duration of 5.12 ms, and B_1 amplitude of 750 Hz. IR scans had only four repetitions (two for reference scans), equaling a total scan time of 1:24 min. In both cases, five slices were acquired with an image resolution of 1.7 mm^3 using SENSE iPAT=2 acceleration factor. The TE was 30 ms, TRs were 2 and 3 s for MT and IR experiments, respectively. A reference MGRE sequence with TR 0.4 s, TE of 4.0 ms, 8 echoes with echo spacing of 0.9 ms, the same resolution as the EPI scans and total scan time of 44 s, was scanned immediately after the MT and IR experiments. This MGRE sequence served as reference to reconstruct the accelerated EPI scans.

4.3.3 Data processing

All scans were in axial orientation, co-planar with AC–PC to cover the corpus callosum. The MT and IR scans were aligned using in-plane registration for each session. Since the scans were taken back-to-back, little movement was expected. EPI reference images were used to draw white matter ROIs in the bilateral optic radiation (OR), splenium (SCC) and genu (GCC) of the corpus callosum, and a bilateral mid-frontal white matter region (FLWM). ROI positioning was checked for each EPI scan type, and edited if necessary to avoid artifacts from motion or susceptibility distortion. Scan repetitions were averaged for each image type to maximize SNR.

By analyzing MT and IR images co-jointly, we were able to estimate MT exchange over time (t) using a bi-exponential model [101,102]. From this, we calculated the MP pool fraction, or f_{MT}. All image reconstruction and processing was done using custom scripts written in IDL version 8.6 (Exelis Visual Information Solutions, Boulder, CO, USA).

4.3.4 Executive function assessments

Participants completed executive function (EF) measures as part of a larger testing battery administered outside the scanner at each study visit. From these we chose two computer-based EF tests for this project: 1) Trail-making Test, Part B (TMT-B), and 2) the Cambridge Neuropsychological Test Automated Battery (CANTAB) Spatial Working Memory (SWM) test. The outcome measures were selected as having the greatest fraction of participants with improved performance at Time 2 relative to Time 1, with 71% for TMT-B and 66% for SWM. Descriptive statistics for EF measures are reported in Table 4.3.

TMT-B is a test of set-shifting, which is the ability to divert or alternate attention between two rules or tasks [152–154]. Participants were instructed to connect a scrambled series of numbers and letters as quickly and accurately as possible. If an error was made, it had to be corrected before finishing the test. The main outcome measure was time (seconds) to finish connecting the sequence, with errors contributing to an increase in total time.

SWM measures the ability to hold, manipulate and update spatial information during a task [154,155]. Participants were instructed to collect a token hidden within a set of boxes. If a box had once contained a token, it would not be reused in subsequent trials. Participants were also told that they should not select a box more than one time during an individual trial. Violation of either rule resulted in a between or within search error penalty. The task started with 3 boxes per

trial, and increased in difficulty to 4, 6, and 8 box trials. The aim of this test was to quantify their ability to successfully adopt a systematic search strategy. Strategy scores (1 = best, 37 = worst) were calculated using 6 and 8 box trial performance.

4.3.4 Statistical analyses

Mean values were compared between time points for all longitudinal measures (demographics, f_{MT}, and EF). Effect size was reported as Hedge's g, which is recommended to correct for positive bias in small samples [119,156]. In addition, common language effect size (CL) was used to express the likelihood that the mean of Time 2 was different from Time 1 for any given participant [119].

Pearson's correlation coefficients were computed to assess the relationship between age-adjusted changes f_{MT} and physical maturation (PDS scale, BMI). Pubertal status coincides with improvements in cognition [34], and timing of puberty has been linked to positive correlations in regional white matter development, such as splenium of corpus callosum [157]. Conversely, increased BMI, particularly for overweight and obese adolescents, has been linked to deficits in executive control, inhibitory control, and working memory [158]; and both global and regional decreases in white matter imaging studies [159,160]. By correlating these measures with f_{MT}, we examined the potential for indirect effects on the relationship of f_{MT} and EF.

Simple linear regression was used to examine age-related change (Time 2 – Time 1/(Age 2 – Age 1) in EF in relation to f_{MT} using the following equation:

$$EF_i = \beta_0 + \beta_1 f_{MT,i} + \varepsilon_i$$

where EF_i is one of the executive function outcome measures, β_0 is the intercept, and β_1 is the slope of the regression line. Model error, or ε_i, is the deviation of each data point $(EF_i, f_{MT,i})$

from the fitted values. We specified a regression model for each combination of EF measure (TMT-B, Spatial Working Memory), and each f_{MT} ROI (OR, SCC, GCC, FLWM). Thus, eight regression analyses were conducted; each testing if the change in f_{MT} impacted the change in EF. Additional predictors, such as sex, were considered for use in multiple linear regression models. However, these data will not be presented as there were no main effects from the eight simple regression models (see Results). R software was used for all statistical analyses [161,162].

4.4 Results

Adolescents had mean differences in age from Time 1 to Time 2 of ~ 18 months, with increased PDS scores indicating significant pubertal maturation during this short timeframe ($t_{(53)} = 4.56$, $p < 0.000$, $t_{(51)} = 7.41$, $p < 0.000$, respectively). Raw BMI scores were also significantly increased, however, these changes were within the typical range when adjusting for age and sex (BMI, %). Figure 4.1 shows distribution of f_{MT} values at both time points (1A) and the change in f_{MT} (1B) for each ROI. Estimates of f_{MT} exhibited the expected posterior to anterior progression in terms of increasing myelin. In addition, the standard deviation as percentage of the mean ranged from 5-6% of total at Time 1 and ~6-7% at Time 2.

There were 43 participants (83%) with increased PDS scores; whereas 5 had no change, and 4 had decreased scores. The PDS has limited specificity due to the nature of self-report, and small deltas in decreased scores were likely due to errors in reporting. At Time 1, only one female participant reported full maturity (PDS = 4), whereas at Time 2, there were three female participants with maximum scores. The PDS scale is subject to a ceiling effect (PDS = 4), but this was not the case for this cohort. There were 41 participants (75%) with increased BMI scores and 14 with decreased scores. For Time 1, 27% of participants were overweight or obese,

while only 22% at Time 2. ROI-based measures of f_{MT} did not correlate with changes in PDS or BMI.

The f_{MT} in FLWM was increased at Time 2 (M = 0.245, SD = 0.015) versus Time 1 (M = 0.239, SD = 0.013), $t_{(49)} = 3.19$, p = 0.003 (see Table 4.2 for the statistical results from all ROIs). There were 31 total participants, or ~ 60%, that had an increase for this region (see Table 4.2 for data in all ROIs). The *p*-value was statistically significant at a Bonferoni-corrected level of $p < 0.0125$. However, effect size (Hedges's g = 0.36) was small to medium, with a CL likelihood estimate of only 67%. SCC, GCC, and OR did not show a significant increase between time points. The smallest true effect size (i.e., the minimal detectable effect, or MDE) was calculated to determined if this sample was reasonable powered to detect an effect of this magnitude. The MDE for a paired, one-tail t-test (assuming an increase) of 50 subjects using conventional cut off values (power = 80%, alpha = 0.5%) was 0.36. This is equivalent to the observed effect for FLWM.

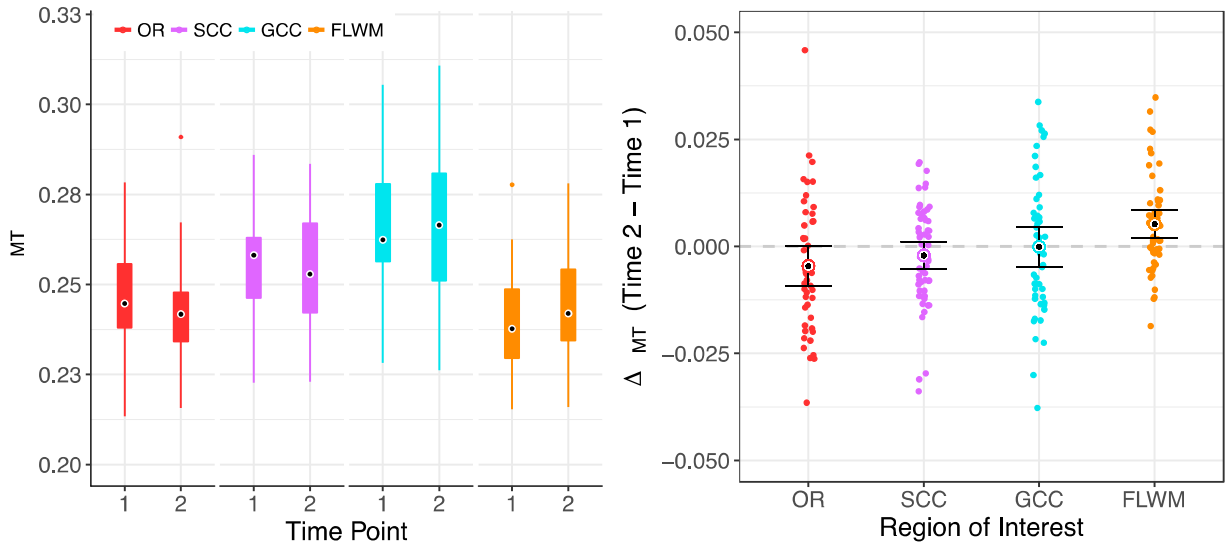

Figure 4.1 Distribution and difference plot of longitudinal f_{MT}. (A) Box plots comparing the distribution of f_{MT} for each ROI measured at Time 1 and Time 2. (B) Difference plot of f_{MT} Time 2 – f_{MT} Time 1 for each paired subject by ROI. The dashed horizontal line (grey) corresponds to no difference. Mean difference for each ROI is shown as a filled circle with error bars set at the 95% confidence interval.

Table 4.2 Descriptive statistics of longitudinal f_{MT}. Mean ± SD are reported for optic radiation, splenium, genu, and frontal white matter ROIs. Significance level was set using a Bonferroni-correction for multiple tests, $p < 0.0125$ ($p < 0.05/4$ ROIs). Paired sample t-tests were tested for each ROI reported as the *t*-statistic and *df* (N-1). CI is the 95% confidence interval of the mean difference. Effect size is reported as Hedge's g. CL is the common language effect size.

ROI	Time 1	Time 2	*t* (df)	*p*	95% CI	Effect size, *g*	CL (%)
OR	0.247 ± 0.013	0.242 ± 0.015	1.97 (45)	0.055	[-0.009, 0.000]	0.32	61%
SCC	0.256 ± 0.014	0.253 ± 0.015	1.31 (55)	0.194	[-0.005, 0.001]	0.14	57%
GCC	0.267 ± 0.017	0.267 ± 0.020	0.06 (48)	0.951	[-0.005, 0.005]	0.01	50%
FLWM	0.239 ± 0.013	0.245 ± 0.015	3.19 (49)	0.003*	[0.002, 0.008]	0.36	67%

The results of the statistical analyses for the executive function tests are shown in Table 4.3 and as expected both TMT-B and SWM had a significant mean decrease in their scores, which corresponds to an improvement in performance from Time 1 to Time 2. Even so, these were small effects with only a ~65% likelihood of change.

Table 4.3 Descriptive statistics of longitudinal executive function. Mean ±SD are reported for Trail Making Test B and Spatial Working Memory. Paired, two-sample t-tests were tested for each group as shown by the *t*-statistic and *df* (N-1). CI is the 95% confidence interval of the mean difference. Effect size is reported as Hedge's g and CL is the common language effect size.

ECF	Time 1	Time 2	*t* (df)	*p*	95% CI	Effect size, *g*	CL (%)
TMT-B	55.08 ± 17.98	48.74 ± 13.93	3.02 (51)	<0.004	[-10.56, -2.13]	0.39	66%
SWM	30.96 ± 5.82	28.98 ± 6.75	2.64 (49)	0.011	[-3.49, -0.47]	0.31	65%

Linear regression was used to test the association of f_{MT} from each ROI with either TMT-B or SWM. As shown in Figure 4.2, there were no significant correlations of the change in f_{MT} and change in either EF measure. Based on these results, no additional regression models were tested.

Figure 4.2 Scatterplot of executive function and f_{MT} for each ROI. Regression equation and r^2 values are included on each plot.

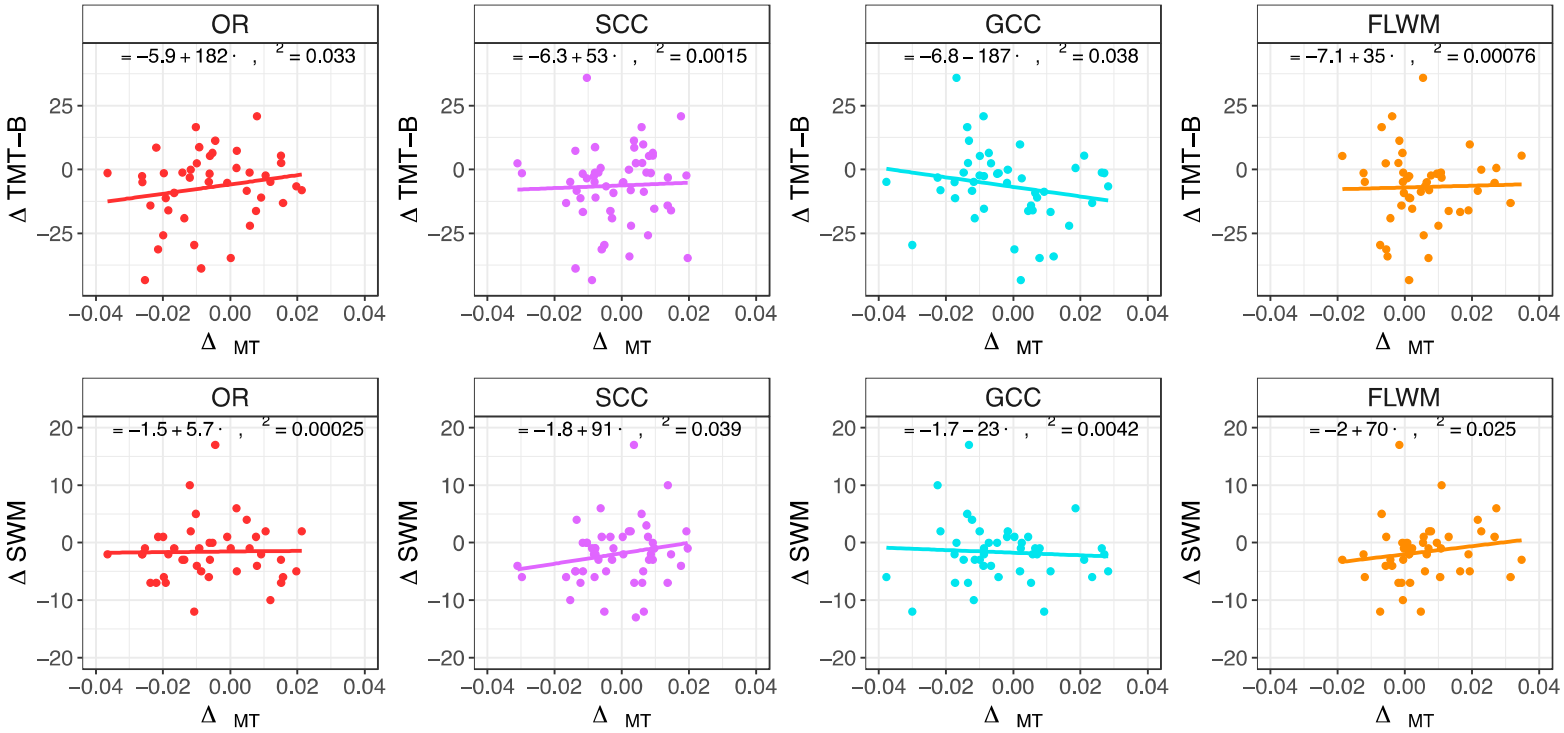

4.5 Discussion

The aim of this study was to investigate adolescent white matter development as it relates to physical and cognitive maturation using a newly developed MT imaging technique. Different regions reach "peak" levels of maturation at different rates as defined by a plateau in these trajectories [35]. In this study, FLWM had the lowest mean f_{MT} values in comparison to other regions; consistent with a delayed myelination in frontal white matter. We observed a significant change from Time 1 to Time 2 for FLWM with approximately 60%, of participants having increased f_{MT} at Time 2. The average percent increase in FLWM was ~5% for participants with positive deltas, and ~2.5% overall. Given the small change in f_{MT} with age, it was not surprising that regression analyses for f_{MT} were not predictive of the improvement in either measure of executive function.

Physical characteristics, such as pubertal status and body mass, have been implicated as important factors for adolescent brain development. Puberty involves both hormonal and physical changes, and typically starts at age 12 for girls and 14 for boys with large variation between individuals (~5 years) [163]. Many conflicting reports exist for sex- or hormone-specific effects on white matter, although most findings in children and adolescents have involved the corpus callosum [164–166]. The corpus callosum is topographically organized to facilitate efficient inter-hemispheric signaling to all lobes of the brain [11]. For this study, we included the splenium, a posterior segment connecting primarily visual cortices, and the genu, an anterior segment connecting prefrontal cortices [11,167]. We did not find any associations in regional f_{MT} with the puberty scale (PDS), possibly as subjects were at or near full sexual maturity by Time 2. Participants also experienced rapid increases in height and weight typical for adolescents. In particular for this cohort, there were 27% and 22% overweight or obese participants at Time 1

and Time 2, respectively. Previous studies have shown an inverse relationship of BMI to global measures of white matter, in addition to posterior corpus callosum and association tracts [168]; however, we did not observe this in the four regions included for this study.

The final comparison was to test if f_{MT} was predictive for either measure of EF. Several cross-sectional studies have reported regional variations in white matter are related to functional specialization during adolescence [169]. In recent longitudinal study (ages 6-25), visuo-spatial working memory was correlated with BOLD contrast in both frontal and parietal regions; in addition, working memory capacity was correlated to white matter tracts associated with or connecting these regions [129]. We hypothesized that f_{MT} of frontal lobe and genu would predict performance in set-shifting and strategy scores. This was not observed; however, the changes in EF and their effect sizes were small over this age range. Combined with the small effects in f_{MT}, we had limited power for detecting a relationship between these measures.

As seen from these comparisons, detecting developmental effects in a longitudinal study can be challenging, as changes within individuals are small (especially over a limited age range), and depend greatly on the precision of technique. Adolescent maturation is an undoubtedly complex process, as studies have suggested hormones, body size, sex, and many external factors, such as peer relationships and nutrition, may interact or predict already subtle individual effects [159,163,170,171]. Therefore, without a large sample, it is difficult to have sufficient power for teasing apart the anatomical and functional correlates of typical adolescent development. However, the percent increase in FLWM f_{MT} was found to be similar to reported DTI white matter metrics in a longitudinal study. For participants ages five to twenty five, investigators reported within subject change was on the order of 4-7% across multiple white matter tracks, compared to precision estimates of 1.4-3.2% [35]. Based on these ranges, the ~2.5% increase in FLWM is certainly

feasible for the age range we studied. In addition, the effect size related to change in FLWM corresponded to a minimum possible effect for this sample size (for 80% power, and alpha = 0.05). By going beyond the p-value, these effects indicate f_{MT} may indeed be sensitive to subtle change during adolescent development.

4.5.1 Conclusions

We used a recently developed MT technique and found a small but significant increase in f_{MT} (~ 2.5%) in the frontal lobe white matter over the span of ~18 months in a healthy sample of adolescents. Unfortunately, this increase was not significantly associated with the improvement in performance in two measures of executive function. We believe the f_{MT} may be useful in future longitudinal studies, although expanding the age range and sample size may be necessary to investigate how these small changes are related to cognitive development.

Chapter V. Discussion

5.1 Concluding remarks and future directions

The objectives of this thesis were to characterize and apply two novel myelin-imaging techniques for the study of adolescent brain development. The primary challenges were addressing the reproducibility and sensitivity of these techniques, selecting the best candidate to detect small effects during development, and interpreting longitudinal results in the context of former studies.

5.1.1 Importance of myelin

From the first paragraph of this dissertation, I sought to highlight the vast, and relatively uncharted territory that is the human brain. Neural networks are intensely interconnected, and the dynamics between them are constantly changing in response to a genetic pattern of development, environmental factors, and new learning experiences. Over the last century, myelin has emerged as a critical, and malleable part of these networks. The adaptability of myelin has been linked to improvements in the efficiency and synchronous optimization of brain function throughout development. While these features are advantageous for fine-tuning brain function, the metabolic demands of myelin make it vulnerable to various stressors and disease. As such, it is important to characterize myelin in the ever-changing brain, to improve our understanding of healthy

development in individuals, and translate these findings to the targeted treatment of disease processes.

5.1.2 MRI and myelin imaging

Throughout modern history, advances in imaging technologies have led to exciting new discoveries that push our knowledge of the physical world forward. Magnetic resonance imaging (MRI) is indisputably such an advance, allowing us to observe the inner workings of a living, complex biological system with unprecedented detail. MRI technology was first implemented in the early 1980's for diagnostic imaging, and since the early 1990's the number of neuroscience research studies using MRI has increased exponentially. There are several key factors related to this growth; for example, it is noninvasive and safe for most people, and it produces high quality visualization of soft tissues throughout the body. Since the early days of MRI, extensive effort has been made to improve the efficiency of acquisition and the quality of the images. In addition, and importantly for imaging of myelin, numerous techniques have been applied to extract more sensitive and specific features related to tissue contrast.

It is important to remember that MRI does not directly measure the cellular components of brain tissue. Neurons, glial cells, and of course, myelin membranes, are much, much smaller than a typical imaging voxel. However, the brain is conveniently organized into low fat (gray matter) and high fat (white matter) regions, with distinct anatomical features that are sensitive to MRI. For this thesis, I employed two techniques, myelin water imaging and magnetization transfer imaging, with enhanced sensitivity to obtain sub-voxel tissue information.

5.1.3 General findings

In Chapter 2, multiple gradient echo (MGRE) MRI was used to measure T_2* decay curves in white matter regions of interest. T_2* is sensitive to disturbances, or inhomogeneities, in the main magnetic field of the MRI machine. As such, these signals reflect the small, but detectable effect of sub-voxel inhomogeneities due to the magnetic susceptibility of certain tissues. The high lipid content and multi-layered structure of myelin have been shown to contribute to these effects, which can be modeled to extract an indirect estimate of myelin content in a voxel. Stronger magnetic fields produce enhanced susceptibility contrast, as measured by faster T_2* signal decay and larger frequency offsets. Chapter 2 investigated the application of MGRE imaging for detecting myelin at two field strengths of 3 and 7 tesla (T). Experiments at 7 T (i.e., stronger magnet) were used as a benchmark for performance at 3 T. This particular approach to imaging myelin has gained interest at 3 T, as it is complementary to established techniques such as diffusion tensor imaging (DTI) and provides unique information for characterizing myelin content. In addition, 3 T MRI (or < 3 T) is more commonly available, and used in the majority of clinical and research applications.

A multi-exponential model was fit to T_2* signal decay curves to describe the contributions of distinct tissue compartments, attributed to myelin, axonal and interstitial water. The relative myelin content, or myelin water fraction, was defined as the fraction of signal attributed to myelin (fast T_2*, large frequency offset) to that of all water sources in the voxel. Model fitting at 3 T was found to be imprecise, which was due to the lack of sensitivity to susceptibility effects at this field strength. The 7 T application was indeed sensitive to each component; however, the human results were not plausible for expected

myelin content in healthy adults. This was a surprise, and likely due to the presence of artifact due to the incorrect tuning of scanner gradients.

While Chapter 2 was conclusive as to the poor reliability of this technique at 3 T, model fitting still returns "reasonable" average values for the myelin water fraction. Reasonable is in quotes, as these estimates are based on what is previously published in the literature. There is no reference standard, or direct quantification as to what the myelin water fraction should be for various tissue types in living human brain. Post-mortem studies have shown high correlation with these values, but ultimately do not correspond to accurate or even specific estimates of myelin content. Even so, reasonable estimates are based on biological observations, such that myelin membranes have ~40% water throughout the multi-layer sheath. We can construct models based on estimated water content to extrapolate various effects, but this is difficult to generalize across the brain. In addition, these estimates are based on an aggregate signal, and subtle differences within a voxel, such as the addition of a few new internodes or myelin layers, may not be detectable with this approach. This can be problematic for future research, as promising new techniques get picked up for their purported specificity to myelin, irrespective of certain performance metrics. The work in Chapter 2 was an attempt to validate the use of these techniques and found that at 3 T the MGRE technique is very sensitive to even small amounts of noise and thus casts doubt on whether it can be used to reliably detect myelin water estimates.

The work in Chapter 3 delves into the reliability of MGRE-based myelin imaging, in contrast with a second myelin-sensitive technique using magnetization transfer (MT) imaging. The primary goal was to compare the reproducibility of each method in a large

sample, to generalize these findings for potential clinical and research applications. For the MT approach, a novel pulse sequence was applied to measure the transient change in magnetization between a non-water, macromolecular proton (MP) pool and a free water proton (WP) pool. The high lipid content of myelin membranes is a large contributor to the MP content in tissue. The relative exchange between each WP and MP can be modeled to extract MP pool size, which is used as an indirect measure of myelin content. While both techniques in this study have been recently developed, the basic principles underlying multi-component relaxation models and two-pool model of magnetization have been compared in previous studies to estimate myelin content. To summarize, the MGRE-based myelin estimate was highly susceptible to measurement error. The MT-based myelin estimate was robust to measurement error, and thus reproducible in this context. Using the variability measured from these data, we calculated the number of subjects that would be necessary to detect a small increase in myelin content. Not surprisingly, the myelin water method needed an unreasonable number of subjects to detect any effect with high confidence, while the MT approach was sensitive to the difference with only a small number of subjects.

In Chapter 4, the MT approach was used to study myelin development in a longitudinal adolescent cohort over the span of ~18 months. Previous studies have shown delayed maturation in association areas and white matter tracts throughout adolescence and into adulthood [11,32]. As such, we hypothesized to find increased myelin content in anterior white matter regions associated with the pre-frontal cortices. A small yet significant increase in myelin content (~2.5%) was observed in frontal white matter, which was comparable in magnitude to a longitudinal MRI study using diffusion tensor

imaging [35]. In addition, MT-based myelin estimates were found to be precise for this cohort, as there were no changes greater than 15% in any white matter region. As such, the MT approach may be useful for future longitudinal studies to study myelin maturation in development.

5.1.4 So what's all the noise about?

The techniques presented in this thesis were evaluated in terms of their applicability for future developmental studies. The MT approach was determined to have superior levels of precision, and which may be applied for future experiments. However, researchers may still fall into the trap of perceived specificity for one technique over another. This may be partially due to branding, as myelin water sounds much better than measuring a non-specific bound proton fraction. There is some merit to this, as MT estimates are based on the assumption that myelin is the dominant source of MPs in white matter. This assumption may be confounded in certain situations, such as inflammation or edema as observed in aging and some diseases. Another approach to interpreting these results is to reexamine the role and source of measurement error.

A common misperception, and one formerly held by this author, is that measurement error, i.e., uncontrolled variation in data, will diminish statistical effects. For example, many believe that if a significant result is found from noisy data, it must indicate the true effect is larger than what was observed from the study. This interpretation seems intuitive, but is not always the case, especially in measurements with high error levels. Errors can actually exaggerate effect size and are partially to blame for the oft-cited science replication crisis [172]. Measurement error is particularly insidious for

small sample sizes, and is propagated when considering multiple predictors and complex study designs. Measurement error can arise from many sources, such as data acquisition, preprocessing methods, analysis techniques, statistical methods, and even researcher bias. Therefore, the reliability and stability of measurements is critical for making correct inferences as to the true nature of an effect.

Appendix: Supplementary Materials

Table 3.S1 Average model parameters for each WM ROI. Data was excluded from some individual ROIs due to localized artifact. (A) For MW, three-component fitting results are shown, where A_n is the relative amplitude (a.u.), $R^*_{2,n}$ the relaxation rate (Hz), f_n the frequency shift (ppm), and φ the phase offset (Hz). (B) For MT, f is the MP fraction (f_{MT}), $R_{1,WP}$ the relaxation rate (Hz) of WP, and k_{WM} and k_{MW} are exchange rate constants relative to WP and MP pool size. The $R_{1,MP}$ (4 Hz) and $S_{MP}(0)$ (0.88) were assumed to be the same values for all subjects.

A. Myelin water parameters

ROI	N	A_1	$R^*_{2,1}$	f_1	A_2	$R^*_{2,2}$	f_2	A_3	$R^*_{2,3}$	f_g	φ
OR	59	0.16	85.8	0.07	0.40	15.1	-0.02	0.53	17.3	0.01	-0.1
SCC	61	0.13	82.3	0.07	0.36	12.0	-0.02	0.58	20.1	0.01	-0.1
GCC	61	0.08	66.5	0.10	0.38	15.0	-0.02	0.61	21.5	0.01	-0.1
FLWM	59	0.09	63.2	0.06	0.42	15.9	-0.02	0.55	17.5	0.01	0.0

B. Magnetization transfer parameters

ROI	N	f	$R_{1,WP}$	k_{WM}	k_{MW}
OR	72	0.255	0.375	2.06	6.02
SCC	80	0.257	0.474	2.46	7.14
GCC	72	0.274	0.366	2.64	6.98
FLWM	74	0.247	0.386	2.32	7.07

References

1. Ranvier L-A. *Leçons Sur l'Histologie Du Système Nerveux*. Paris: Librairie Savy; 1878.
2. Azevedo FAC, Carvalho LRB, Grinberg L, et al. Equal numbers of neuronal and nonneuronal cells make the human brain an isometrically scaled-up primate brain. *J Comp Neurol*. 2009;513:532-541. doi:10.1002/cne.21974.
3. Turner R, Geyer S. Comparing like with like: the power of knowing where you are. *Brain Connect*. 2014;4(7):547-557. doi:10.1089/brain.2014.0261.
4. von Bartheld CS, Bahney J, Herculano-Houzel S. The search for true numbers of neurons and glial cells in the human brain: A review of 150 years of cell counting. *J Comp Neurol*. 2016;524:3865-3895. doi:10.1002/cne.24040.
5. Virchow R. Ueber das granulirte Aussehen der Wandungen der Gehirnventrikel. *Allg Z Psychiat*. 1846;3:242-250.
6. Baumann N, Pham-Dinh D. Biology of oligodendrocyte and myelin in the mammalian central nervous system. *Physiol Rev*. 2001;81(2):871-927.
7. Hodgkin A, Huxley A. A quantitative description of membrane current and its application to conduction and excitation in nerve. *J Physiol*. 1952;117:500-544.
8. Young J. The functioning of the giant nerve fibres of the squid. *J Exp Biol*. 1938:170-185.
9. Salzer JL, Zalc B. Myelination. *Curr Biol*. 2016;26:R971-975. doi:10.1016/j.cub.2016.07.074.

10. Fields RD. White matter in learning, cognition and psychiatric disorders. *Trends Neurosci*. 2008;31:361-370. doi:10.1016/j.tins.2008.04.001.

11. Aboitiz F, Scheibel AB, Fisher RS, Zaidel E. Fiber composition of the human corpus callosum. *Brain Res*. 1992;598(1-2):143-153. doi:10.1016/0006-8993(92)90178-C.

12. Axer H. Microstructural analysis of human white matter architecture using polarized light imaging: Views from neuroanatomy. *Front Neuroinform*. 2011;5(November):1-12. doi:10.3389/fninf.2011.00028.

13. Liewald D, Miller R, Logothetis N, Wagner HJ, Schüz A. Distribution of axon diameters in cortical white matter: an electron-microscopic study on three human brains and a macaque. *Biol Cybern*. 2014;108(5):541-557. doi:10.1007/s00422-014-0626-2.

14. Chomiak T, Hu B. What is the optimal value of the g-ratio for myelinated fibers in the rat CNS? A theoretical approach. *PLoS One*. 2009;4(11). doi:10.1371/journal.pone.0007754.

15. ffrench-Constant C, Colognato H, Franklin RJM. The mysteries of myelin unwrapped. *Science*. 2004;304:688-689.

16. Paus T, Toro R, Nave K. Could sex differences in white matter be explained by g-ratio? *Front Neuroanat*. 2009;3:1-7. doi:10.3389/neuro.05.014.2009.

17. Schmitt F, Bear R. The optical properties of vertebrate nerve axons as related to fiber size. *J Cell Physiol*. 1937:261-273.

18. Rushton WAH. A theory of the effects of fibre size in medullated nerve. *J Physiol*. 1951;115:101-122.

19. Tomassy GS, Berger DR, Chen H-H, et al. Distinct profiles of myelin distribution along single axons of pyramidal neurons in the neocortex. *Science*. 2014;344:319-324. doi:10.1126/science.1249766.

20. Micheva KD, Wolman D, Mensh BD, et al. A large fraction of neocortical myelin ensheathes axons of local inhibitory neurons. *Elife*. 2016:1-29. doi:10.7554/eLife.15784.

21. Buzsaki G, Draguhn A. Neuronal oscillations in cortical networks. *Science.* 2004;304:1926-1930.

22. Geren BB. The formation from the schwann cell surface of myelin in the peripheral nerves of chick embryos. *Exp Cell Res*. 1954;7:558-562.

23. Bunge MB, Bunge RP, Pappas GD. Electron microscopic demonstration of connections between glia and myelin sheaths in the developing mammalian central nervous system. *J Cell Biol*. 1962;12(2):448-453.

24. Bunge R. Glial cells and the central myelin sheath. *Physiol Rev*. 1968;48(1):197-251. http://www.ncbi.nlm.nih.gov/pubmed/4866614.

25. Peters A. The formation and structure of myelin sheaths in the central nervous system. *J Biophys Biochem Cytol*. 1960;(10):431-446.

26. Snaidero N, Simons M. The logistics of myelin biogenesis in the central nervous system. *Glia*. 2017;65:1021-1031. doi:10.1002/glia.23116.

27. Hildebrand C, Remahl S, Persson H, Bjartmar C. Myelinated nerve fibres in the CNS. *Prog Neurobiol*. 1993;40(3):319-384. doi:10.1016/0301-0082(93)90015-K.

28. Caspar D, Kirschner DA. Myelin membrane structure at 10 A resolution. *Nat New Biol*. 1971;231(5).

29. De Felici M, Felici R, Ferrero C, Tartari A, Gambaccini M, Finet S. Structural characterization of the human cerebral myelin sheath by small angle x-ray scattering. *Phys Med Biol*. 2008;53(20):5675-5688. doi:10.1088/0031-9155/53/20/007.

30. Kirschner DA, Caspar DLD. Comparative diffraction studies on myelin membraines. *Ann N Y Acad Sci*. 1972;195(1):309-320.

31. Flechsig P. Anatomie des menschlichen Gehirns und Rückenmarks auf myelogentischer Grundlage. 1920:9-37.

32. Yakovlev PI, Lecours A-R. The myelogenetic cycles of regional maturation of the brain. In: *Regional Development of Brain in Early Life*. ; 1967:3-70.

33. Miller DJ, Duka T, Stimpson CD, et al. Prolonged myelination in human neocortical evolution. *Proc Natl Acad Sci*. 2012;109(41):16480-16485. doi:10.1073/pnas.1117943109.

34. Blakemore S-J, Choudhury S. Development of the adolescent brain: Implications for executive function and social cognition. *J Child Psychol Psychiatry*. 2006;47:296-312. doi:10.1111/j.1469-7610.2006.01611.x.

35. Lebel C, Beaulieu C. Longitudinal development of human brain wiring continues from childhood into adulthood. *J Neurosci*. 2011;31(30):10937-10947. doi:10.1523/JNEUROSCI.5302-10.2011.

36. Bartzokis G. Alzheimer's disease as homeostatic responses to age-related myelin breakdown. *Neurobiol Aging*. 2011;32:1341-1371. doi:10.1016/j.neurobiolaging.2009.08.007.

37. Douaud G, Groves AR, Tamnes CK, et al. A common brain network links

development, aging, and vulnerability to disease. *Proc Natl Acad Sci*. 2014;111:17648-17653. doi:10.1073/pnas.1410378111.

38. Flynn SW, Lang DJ, Mackay AL, et al. Abnormalities of myelination in schizophrenia detected in vivo with MRI, and post-mortem with analysis of oligodendrocyte proteins. *Mol Psychiatry*. 2003;8:811-820. doi:10.1038/sj.mp.4001337.

39. Pusic AD, Kraig RP. Youth and environmental enrichment generate serum exosomes containing miR-219 that promote CNS myelination. *Glia*. 2014;62:284-299. doi:10.1002/glia.22606.

40. Kwik-Uribe CL, Gietzen D, German JB, Golub MS, Keen CL. Chronic marginal iron intakes during early development in mice result in persistent changes in dopamine metabolism and myelin composition. *J Nutr*. 2000;130(11):2821-2830. http://www.ncbi.nlm.nih.gov/pubmed/11053527.

41. Rosato-Siri M V, Badaracco ME, Ortiz EH, et al. Oligodendrogenesis in iron-deficient rats: Effect of apotransferrin. *J Neurosci Res*. 2010;88(8):1695-1707. doi:10.1002/jnr.22348.

42. Todorich B, Pasquini JM, Garcia CI, Paez PM, Connor JR. Oligodendrocytes and myelination: the role of iron. *Glia*. 2009;57(5):467-478. doi:10.1002/glia.20784.

43. McKenzie IA, Ohayon D, Li H, et al. Motor skill learning requires active central myelination. *Science*. 2014;346:318-322. doi:10.1126/science.1254960.

44. Scholz J, Klein MC, Behrens TEJ, Johansen-Berg H. Training induces changes in white-matter architecture. *Nat Neurosci*. 2009;12(11):1370-1371. doi:10.1038/nn.2412.

45. Braitenberg V. Brain size and number of neurons: An exercise in synthetic neuroanatomy. *J Comput Neurosci*. 2001;10:71-77.

46. Giedd JN, Raznahan A, Alexander-Bloch A, Schmitt E, Gogtay N, Rapoport JL. Child Psychiatry Branch of the National Institute Mental Health Longitudinal Structural Magnetic Resonance Imaging Study of Human Brain Development. *Neuropsychopharmacology*. September 2014:1-7. doi:10.1038/npp.2014.236.

47. Ribeiro PFM, Ventura-Antunes L, Gabi M, et al. The human cerebral cortex is neither one nor many: Neuronal distribution reveals two quantitatively different zones in the gray matter, three in the white matter, and explains local variations in cortical folding. *Front Neuroanat*. 2013;7:1-20. doi:10.3389/fnana.2013.00028.

48. Duyn JH, van Gelderen P, Li T-Q, de Zwart JA, Koretsky AP, Fukunaga M. High-field MRI of brain cortical substructure based on signal phase. *Proc Natl Acad Sci*. 2007;104(28):11796-11801. doi:10.1073/pnas.0610821104.

49. Oldendorf W, William Oldendorf J. *MRI Primer*. New York, New York: Raven Press; 1991.

50. Paus T, Keshavan M, Giedd JN. Why do many psychiatric disorders emerge during adolescence? *Nat Rev Neurosci*. 2008;9(12):947-957. doi:10.1038/nrn2513.

51. Rooney WD, Johnson G, Li X, et al. Magnetic field and tissue dependencies of human brain longitudinal $^{1}H2O$ relaxation in vivo. *Magn Reson Med*. 2007;57(2):308-318. doi:10.1002/mrm.21122.

52. Basser PJ, Pierpaoli C. Microstructural and physiological features of tissues elucidated by quantitative-diffusion-tensor MRI. *J Magn Reson*. 1996;111:209-219. doi:10.1016/j.jmr.2011.09.022.

53. Jones DK, Cercignani M. Twenty-five pitfalls in the analysis of diffusion MRI data. *NMR Biomed*. 2010;23(7):803-820. doi:10.1002/nbm.1543.

54. Vasilescu V, Katona E, Simplaceanu V, Demco D. Water compartments in the myelinated nerve. III. Pulsed NMR results. *Experientia*. 1978;34:1443–1444. http://link.springer.com/article/10.1007/BF01932339. Accessed October 21, 2014.

55. MacKay A, Whittal K, Adles J, et al. In vivo visualization of myelin water in brain by magnetic resonance. *Magn Reson Med*. 1994;31:673-677.

56. West KL, Does MD. Myelin volume fraction imaging with MRI. *Neuroimage*. 2016. doi:10.1016/j.neuroimage.2016.12.067.

57. Harkins KD, Valentine WM, Gochberg DF, Does MD. In-vivo multi-exponential T_2, magnetization transfer and quantitative histology in a rat model of intramyelinic edema. *NeuroImage Clin*. 2013;2:810-817. doi:10.1016/j.nicl.2013.06.007.

58. Laule C, Leung E, Li DKB, et al. Myelin water imaging in multiple sclerosis: Quantitative correlations with histopathology. *Mult Scler*. 2006;12:747-753.

59. Levesque IR, Giacomini PS, Narayanan S, et al. Quantitative magnetization transfer and myelin water imaging of the evolution of acute multiple sclerosis lesions. *Magn Reson Med*. 2010;63(3):633-640. doi:10.1002/mrm.22244.

60. Andrews T, Lancaster JL, Dodd SJ, Contreras-sesvold C, Fox PT. Testing the three-pool white matter model adapted for use with T_2 relaxometry. *Magn Reson Med*. 2005;454(July 2004):449-454. doi:10.1002/mrm.20599.

61. Du YP, Chu R, Hwang D, et al. Fast multislice mapping of the myelin water fraction using multicompartment analysis of T_2* decay at 3T: A preliminary

postmortem study. *Magn Reson Med*. 2007;58(5):865-870. doi:10.1002/mrm.21409.

62. Alonso-Ortiz E, Levesque IR, Pike GB. MRI-based myelin water imaging: A technical review. *Magn Reson Med*. 2014;0. doi:10.1002/mrm.25198.

63. van Gelderen P, de Zwart JA, Lee J, Sati P, Reich DS, Duyn JH. Nonexponential T_2* decay in white matter. *Magn Reson Med*. 2012;67(1):110-117. doi:10.1002/mrm.22990.

64. Sati P, van Gelderen P, Silva AC, et al. Micro-compartment specific T_2* relaxation in the brain. *Neuroimage*. 2013;77:268-278. doi:10.1016/j.neuroimage.2013.03.005.

65. Duyn JH, Schenck J. Contributions to magnetic susceptibility of brain tissue. *NMR Biomed*. 2016;(February). doi:10.1002/nbm.3546.

66. Schenck J. The role of magnetic susceptibility in magnetic resonance imaging: MRI magnetic compatibility of the first and second kinds. *Med Phys*. 1996;23:815-850.

67. van Gelderen P, Mandelkow H, de Zwart JA, Duyn JH. A torque balance measurement of anisotropy of the magnetic susceptibility in white matter. *Magn Reson Med*. 2014. doi:10.1002/mrm.25524.

68. Wharton S, Bowtell R. Fiber orientation-dependent white matter contrast in gradient echo MRI. *Proc Natl Acad Sci*. 2012;109(45):18559-18564. doi:10.1073/pnas.1211075109.

69. Duyn JH. Frequency shifts in the myelin water compartment. *Magn Reson Med*. 2014;71(6):1953-1955. doi:10.1002/mrm.24983.

70. Randall LO. Chemical topography of the brain. *J Biol Chem*. 1938;124(2):481–488.

71. O'Brien JS, Sampson EL. Lipid composition of the normal human brain: gray matter, white matter, and myelin. *J Lipid Res*. 1965;6(9):537-544.

72. Horch RA, Gore JC, Does MD. Origins of the ultrashort-T_2 ^{1}H NMR signals in myelinated nerve: A direct measure of myelin content? *Magn Reson Med*. 2011;66(1):24-31. doi:10.1002/mrm.22980.

73. Wolff SD, Balaban RS. Magnetization transfer contrast (MTC) and tissue water proton relaxation in vivo. *Magn Reson Med*. 1989;10(1):135-144. http://www.ncbi.nlm.nih.gov/pubmed/2547135.

74. Forsén S, Hoffman RA. Study of moderately rapid chemical exchange reactions by means of nuclear magnetic double resonance. *J Chem Phys*. 1963;39:2892-2901. doi:10.1063/1.1734121.

75. Edzes HT, Samulski ET. Cross relaxation and spin diffusion in the proton NMR of hydrated collagen. *Nature*. 1977;265:521-523.

76. Alexander AL, Hurley SA, Samsonov AA, et al. Characterization of cerebral white matter properties using quantitative magnetic resonance imaging stains. *Brain Connect*. 2011;1:423-446. doi:10.1089/brain.2011.0071.

77. Dortch RD, Li K, Gochberg DF, et al. Quantitative magnetization transfer imaging in human brain at 3 T via selective inversion recovery. *Magn Reson Med*. 2011;66:1346-1352. doi:10.1002/mrm.22928.

78. Soellinger M, Langkammer C, Fazekas F, Ropele S. Fast bound pool fraction mapping using stimulated echoes. *Magn Reson Med*. 2011;66:717-724.

doi:10.1002/mrm.22846.

79. Gochberg DF, Gore JC. Quantitative imaging of magnetization transfer using an inversion recovery sequence. *Magn Reson Med*. 2003;49:501-505. doi:10.1002/mrm.10386.

80. Helms G, Hagberg GE. In vivo quantification of the bound pool T_1 in human white matter using the binary spin – bath model of progressive magnetization transfer saturation. *Phys Med Biol*. 2009;54:N529-N540. doi:10.1088/0031-9155/54/23/N01.

81. Fuhrmann D, Knoll L, Blakemore S-J. Adolescence as a sensitive period of brain development. *Trends Cogn Sci*. 2015;19(10):558-566. doi:10.1111/j.1750-8606.2008.00038.x.

82. Lee FS, Heimer H, Giedd JN, et al. Adolescent mental health— Opportunity and obligation. *Science*. 2014;346(6209):547-549.

83. Tamnes CK, Østby Y, Fjell AM, Westlye LT, Due-Tønnessen P, Walhovd KB. Brain maturation in adolescence and young adulthood: Regional age-related changes in cortical thickness and white matter volume and microstructure. *Cereb Cortex*. 2010;20(March):534-548. doi:10.1093/cercor/bhp118.

84. Mills KL, Tamnes CK. Methods and considerations for longitudinal structural brain imaging analysis across development. *Dev Cogn Neurosci*. 2014;9:172-190. doi:10.1016/j.dcn.2014.04.004.

85. Meyers SM, Laule C, Vavasour IM, et al. Reproducibility of myelin water fraction analysis: A comparison of region of interest and voxel-based analysis methods. *Magn Reson Imaging*. 2009;27(8):1096-1103. doi:10.1016/j.mri.2009.02.001.

86. Levesque IR, Chia CLL, Pike GB. Reproducibility of in vivo magnetic resonance imaging-based measurement of myelin water. *J Magn Reson Imaging*. 2010;32:60-68. doi:10.1002/jmri.22170.

87. Hwang D, Kim D-H, Du YP. In vivo multi-slice mapping of myelin water content using T_2* decay. *Neuroimage*. 2010;52(1):198-204. doi:10.1016/j.neuroimage.2010.04.023.

88. Prasloski T, Rauscher A, Mackay AL, et al. Rapid whole cerebrum myelin water imaging using a 3D GRASE sequence. *Neuroimage*. 2012;63(1):533-539. doi:10.1016/j.neuroimage.2012.06.064.

89. Deoni SCL, Rutt BK, Arun T, Pierpaoli C, Jones DK. Gleaning multicomponent T_1 and T_2 information from steady-state imaging data. *Magn Reson Med*. 2008;60(6):1372-1387. doi:10.1002/mrm.21704.

90. Duyn JH. The future of ultra-high field MRI and fMRI for study of the human brain. *Neuroimage*. 2012;62(2):1241-1248. doi:10.1016/j.neuroimage.2011.10.065.

91. Peters AM, Brookes MJ, Hoogenraad FG, et al. T_2* measurements in human brain at 1.5, 3 and 7 T. *Magn Reson Imaging*. 2007;25:748-753. doi:10.1016/j.mri.2007.02.014.

92. van Gelderen P, de Zwart JA, Starewicz P, Hinks RS, Duyn JH. Real-time shimming to compensate for respiration-induced B0 fluctuations. *Magn Reson Med*. 2007;57(2):362-368. doi:10.1002/mrm.21136.

93. Li X, van Gelderen P, Sati P, de Zwart JA, Reich DS, Duyn JH. Detection of demyelination in multiple sclerosis by analysis of T_2*. *NeuroImage Clin*.

2015;7:709-714. doi:10.1016/j.nicl.2015.02.021.

94. Alonso-Ortiz E, Levesque IR, Pike GB. MRI-based myelin water imaging: A technical review. *Magn Reson Med*. 2014;81:70-81. doi:10.1002/mrm.25198.

95. Nam Y, Lee J. Physiologial noise compensation in gradient echo based myelin water imaging. In: *International Society of Magnetic Resonance in Medicine 23*. Vol 6. ; 2015. doi:10.1002/mrm.25114.

96. Karsa A, Biondetti E, Punwani S, Shmueli K. The effect of large slice thickness and spacing and low coverage on the accuracy of susceptibility mapping. *Proc Intl Soc Mag Reson Med*. 2016.

97. Harkins KD, Xu J, Dula AN, et al. The microstructural correlates of T_1 in white matter. *Magn Reson Med*. 2015;0(February):n/a-n/a. doi:10.1002/mrm.25709.

98. Dula AN, Gochberg DF, Valentine HL, Valentine WM, Does MD. Multiexponential T_2, magnetization transfer, and quantitative histology in white matter tracts of rat spinal cord. *Magn Reson Med*. 2010;63(4):902-909. doi:10.1002/mrm.22267.

99. Vavasour IM, Whittall KP, MacKay AL, Li DKB, Vorobeychik G, Paty DW. A comparison between magnetization transfer ratios and myelin water percentages in normals and multiple sclerosis patients. *Magn Reson Med*. 1998:763-768. http://onlinelibrary.wiley.com/doi/10.1002/mrm.1910400518/abstract.

100. Sati P, Silva AC, van Gelderen P, et al. In vivo quantification of T_2* anisotropy in white matter fibers in marmoset monkeys. *Neuroimage*. 2012;59(2):979-985. doi:10.1016/j.neuroimage.2011.08.064.

101. van Gelderen P, Jiang X, Duyn JH. Effects of magnetization transfer on T_1 contrast

in human brain white matter. *Neuroimage*. 2016;128:85-95. doi:10.1016/j.neuroimage.2015.12.032.

102. van Gelderen P, Jiang X, Duyn JH. Rapid measurement of brain macromolecular proton fraction with transient saturation transfer MRI. *Magn Reson Med*. 2016;0. doi:10.1002/mrm.26304.

103. MacKay AL, Laule C. Magnetic resonance of myelin water: An in vivo marker for myelin. *Brain Plast*. 2016;2:1-21. doi:10.3233/BPL-160033.

104. Hwang D, Du YP. Improved myelin water quantification using spatially regularized non-negative least squares algorithm. *J Magn Reson Imaging*. 2009;30(1):203-208. doi:10.1002/jmri.21783.

105. Graham SJ, Stanchev PL, Bronskill MJ. Criteria for analysis of multicomponent tissue T_2 relaxation data. *Magn Reson Med*. 1996;35:370-378.

106. Wharton S, Bowtell R. Gradient echo based fiber orientation mapping using R_2* and frequency difference measurements. *Neuroimage*. July 2013. doi:10.1016/j.neuroimage.2013.07.054.

107. Duyn JH. Studying brain microstructure with magnetic susceptibility contrast at high- field. *Neuroimage*. 2017. doi:10.1016/j.neuroimage.2017.02.046.

108. Gelman N, Ewing JR, Gorell JM, Spickler EM, Solomon EG. Interregional variation of longitudinal relaxation rates in human brain at 3.0 T: Relation to estimated iron and water contents. *Magn Reson Med*. 2001;45(1):71-79. doi:10.1002/1522-2594(200101)45:1<71::AID-MRM1011>3.0.CO;2-2.

109. Does MD, Beaulieu C, Allen PS, Snyder RE. Multi-component T_1 relaxation and magnetisation transfer in peripheral nerve. *Magn Reson Imaging*.

1998;16(9):1033-1041. doi:10.1016/S0730-725X(98)00139-8.

110. Stikov N, Boudreau M, Levesque IR, Tardif CL, Barral JK, Pike GB. On the accuracy of T_1 mapping: Searching for common ground. *Magn Reson Med*. 2015;73(2):514-522. doi:10.1002/mrm.25135.

111. Varma G, Duhamel G, de Bazelaire C, Alsop DC. Magnetization transfer from inhomogeneously broadened lines: A potential marker for myelin. *Magn Reson Med*. 2014;0:1-9. doi:10.1002/mrm.25174.

112. Jiang X, Gelderen P Van, Duyn JH. Spectral characteristics of semisolid protons in human brain white matter at 7 T. *Magn Reson Med*. 2017;0:1-9. doi:10.1002/mrm.26594.

113. Lebel C, Walker L, Leemans A, Phillips L, Beaulieu C. Microstructural maturation of the human brain from childhood to adulthood. *Neuroimage*. 2008;40(3):1044-1055. doi:10.1016/j.neuroimage.2007.12.053.

114. Fishbein DH, Rose EJ, Darcey VL, Belcher AM, VanMeter JW. Neurodevelopmental precursors and consequences of substance use during adolescence: Promises and pitfalls of longitudinal neuroimaging strategies. *Front Hum Neurosci*. 2016;10(June):296. doi:10.3389/fnhum.2016.00296.

115. Rajan J, Poot D, Juntu J, Sijbers J. Noise measurement from magnitude MRI using estimates of variance and skewness. *Phys Med Biol*. 2010;55. doi:10.1088/0031-9155/55/22/6973.

116. Hutton C, Balteau E, Lutti A, Josephs O, Weiskopf N. Modelling temporal stability of EPI time series using magnitude images acquired with multi-channel receiver coils. *PLoS One*. 2012;7(12):1-10. doi:10.1371/journal.pone.0052075.

117. Kaufman L, Kramer DM, Crooks LE, Ortendahl DA. Measuring signal-to-noise ratios in MR imaging. *Radiology*. 1989;173:265-267. doi:10.1148/radiology.173.1.2781018.

118. Ku HH. Notes on the use of propagation of error formulas. *J Res Natl Bur Stand (1934)*. 1966;70C(4):75-79.

119. Lakens D. Calculating and reporting effect sizes to facilitate cumulative science: A practical primer for t-tests and ANOVAs. *Front Psychol*. 2013;4(November):1-12. doi:10.3389/fpsyg.2013.00863.

120. Faul F, Erdfelder E, Lang AG, Buchner A. G*Power 3: A flexible statistical power analysis program for the social, behavioral, and biomedical sciences. *Behav Res Methods*. 2007;39(2):175-191.

121. Cohen J. *Statistical Power Analysis for the Behavioral Sciences*. Second Edi. Lawrence Erlbaum Associates; 1988.

122. Lankford CL, Does MD. Propagation of error from parameter constraints in quantitative MRI: Example application of multiple spin echo T_2 mapping. *Magn Reson Med*. 2017. doi:10.1002/mrm.26713.

123. Lankford CL, Does MD. On the inherent precision of mcDESPOT. *Magn Reson Med*. 2013;69(1):127-136. doi:10.1002/mrm.24241.

124. Schmierer K, Tozer DJ, Scaravilli F, et al. Quantitative magnetization transfer imaging in postmortem multiple sclerosis brain. *J Magn Reson Imaging*. 2007;26(1):41-51. doi:10.1002/jmri.20984.Quantitative.

125. Wang S, Young KM. White matter plasticity in adulthood. *Neuroscience*. 2013;276:148-160. doi:10.1016/j.neuroscience.2013.10.018.

126. Nave K-A. Myelination and the trophic support of long axons. *Nat Rev Neurosci*. 2010;11(4):275-283. doi:10.1038/nrn2797.

127. Bartzokis G, Lu PH, Heydari P, et al. Multimodal magnetic resonance imaging assessment of white matter aging trajectories over the lifespan of healthy individuals. *Biol Psychiatry*. 2012;72(12):1026-1034. doi:10.1016/j.biopsych.2012.07.010.

128. Nagy Z, Westerberg H, Klingberg T. Maturation of white matter is associated with the development of cognitive functions during childhood. *J Cogn Neurosci*. 2004;16(7):1227-1233. doi:10.1162/0898929041920441.

129. Darki F, Klingberg T. The role of fronto-parietal and fronto-striatal networks in the development of working memory: A longitudinal study. *Cereb Cortex*. 2015;25(6):1587-1595. doi:10.1093/cercor/bht352.

130. Thiebaut de Schotten M, Cohen L, Amemiya E, Braga LW, Dehaene S. Learning to read improves the structure of the arcuate fasciculus. *Cereb Cortex*. 2012;3:1-7. doi:10.1093/cercor/bhs383.

131. Madsen KS, Baaré WFC, Vestergaard M, et al. Response inhibition is associated with white matter microstructure in children. *Neuropsychologia*. 2010;48(4):854-862. doi:10.1016/j.neuropsychologia.2009.11.001.

132. Lenroot RK, Giedd JN. Brain development in children and adolescents: Insights from anatomical magnetic resonance imaging. *Neurosci Biobehav Rev*. 2006;30:718-729. doi:10.1016/j.neubiorev.2006.06.001.

133. Gogtay N, Giedd JN, Lusk L, et al. Dynamic mapping of human cortical development during childhood through early adulthood. *Proc Natl Acad Sci*.

2004;101(21).

134. Jahanshad N, Thompson PM. Multimodal neuroimaging of male and female brain structure in health and disease across the life span. *J Neurosci Res*. 2017;95(1-2):371-379. doi:10.1002/jnr.23919.

135. Ridgway GR, Omar R, Ourselin S, Hill DLG, Warren JD, Fox NC. Issues with threshold masking in voxel-based morphometry of atrophied brains. *Neuroimage*. 2009;44:99-111. doi:10.1016/j.neuroimage.2008.08.045.

136. Ridgway GR, Henley SMD, Rohrer JD, Scahill RI, Warren JD, Fox NC. Ten simple rules for reporting voxel-based morphometry studies. *Neuroimage*. 2008;40:1429-1435. doi:10.1016/j.neuroimage.2008.01.003.

137. Jones DK, Leemans A. Diffusion tensor imaging. *Methods Mol Biol*. 2011;711(2):127-144. doi:10.1007/978-1-61737-992-5_6.

138. Beaulieu C. The basis of anisotropic water diffusion in the nervous system - a technical review. *NMR Biomed*. 2002;15:435-455. doi:10.1002/nbm.782.

139. Choe AS, Stepniewska I, Colvin DC, Ding Z, Anderson AW. Validation of diffusion tensor MRI in the central nervous system using light microscopy: quantitative comparison of fiber properties. *NMR Biomed*. 2012;25(7):900-908. doi:10.1002/nbm.1810.Validation.

140. Genc S, Malpas CB, Holland SK, Beare R, Silk TJ. Neurite density index is sensitive to age related differences in the developing brain. *Neuroimage*. 2017;148:373-380. doi:10.1016/j.neuroimage.2017.01.023.

141. Zhang H, Schneider T, Wheeler-Kingshott CA, Alexander DC. NODDI: Practical in vivo neurite orientation dispersion and density imaging of the human brain.

Neuroimage. 2012;61(4):1000-1016. doi:10.1016/j.neuroimage.2012.03.072.

142. Raffelt DA, Smith RE, Ridgway GR, et al. Connectivity-based fixel enhancement: Whole-brain statistical analysis of diffusion MRI measures in the presence of crossing fibres. *Neuroimage*. 2015;117:40-55. doi:10.1016/j.neuroimage.2015.05.039.

143. Acheson A, Wijtenburg SA, Rowland LM, et al. Reproducibility of tract-based white matter microstructural measures using the ENIGMA-DTI protocol. *Brain Behav*. 2016;(October):e00615. doi:10.1002/brb3.615.

144. Dousset V, Brochet B, Vital A, et al. Lysolecithin-induced demyelination in primates: Preliminary in vivo study with MR and magnetization transfer. *Am J Neuroradiol*. 1995;16:225-231.

145. Whitaker KJ, Vértes PE, Romero-Garcia R, et al. Adolescence is associated with genomically patterned consolidation of the hubs of the human brain connectome. *Proc Natl Acad Sci*. 2016;113(32):201601745. doi:10.1073/pnas.1601745113.

146. Laule C, Vavasour IM, Kolind SH, et al. Magnetic resonance imaging of myelin. *Neurotherapeutics*. 2007;4(3):460-484. doi:10.1016/j.nurt.2007.05.004.

147. Kaufman AS, Wang J-J. Gender, race, and education differences on the K-Bit at ages 4 to 90 years. *J Psychoeduc Assess*. 1992;10(3):219-229. doi:10.1177/073428299201000302.

148. Manuck S, Phillips J, Gianaros P, Flory J, Muldoon M. Subjective socioeconomic status and presence of the metabolic syndrome in midlife community volunteers. *Psychosom Med*. 2010;72(1):35-45. doi:10.1097/PSY.0b013e3181c484dc.Subjective.

149. NCD Risk Factor Collaboration. Trends in adult body-mass index in 200 countries from 1975 to 2014: a pooled analysis of 1698 population-based measurement studies with 19.2 million participants. *Lancet*. 2016;387(10026):1377-1396. doi:10.1016/S0140-6736(16)30054-X.

150. Thamotharan S, Lange K, Zale EL, Huffhines L, Fields S. The role of impulsivity in pediatric obesity and weight status: A meta-analytic review. *Clin Psychol Rev*. 2013;33(2):253-262. doi:10.1016/j.cpr.2012.12.001.

151. Carskadon MA, Acebo C. A self-administered development rating scale for pubertal development. *J Adolesc Heal*. 1993;14:190-195.

152. Misdraji EL, Gass CS. The Trail Making Test and its neurobehavioral components. *J Clin Exp Neuropsychol*. 2010;32(2):159-163. doi:10.1080/13803390902881942.

153. Sanchez-Cubillo I, Periáñez JA, Adrover-Roig D, et al. Construct validity of the Trail Making Test: Role of task-switching, working memory, inhibition/interference control, and visuomotor abilities. *J Int Neuropsychol Soc*. 2009;15:438-450. doi:10.1017/S1355617709090626.

154. Strauss E, Sherman EM, Spreen O. *A Compendium of Neuropsychological Tests*. Third Edit. New York, New Tork: Oxford University Press; 2006.

155. Robbins T, James M, Owens A, Sahakian B, McInnes L, Rabbitt P. Cambridge Neuropsychological Test Automated Battery (CANTAB): A factor analytic study of a large sample of normal elderly volunteers. *Dementia*. 1994;5:266-281.

156. Hedges L V, Olkin I. *Statistical Methods in Meta-Analysis*. San Diego, CA: Academic Press.; 1985. doi:10.2307/1164953.

157. Genc S, Seal ML, Dhollander T, Malpas CB, Hazell P, Silk TJ. White matter

alterations at pubertal onset. *Neuroimage*. 2017;156:286-292. doi:10.1016/j.neuroimage.2017.05.017.

158. Fields SA, Sabet M, Reynolds B. Dimensions of impulsive behavior in obese, overweight, and healthy-weight adolescents. *Appetite*. 2013;70:60-66. doi:10.1016/j.appet.2013.06.089.

159. Schwartz DH, Dickie E, Pangelinan MM, et al. Adiposity is associated with structural properties of the adolescent brain. *Neuroimage*. 2014;103C:192-201. doi:10.1016/j.neuroimage.2014.09.030.

160. Bolzenius JD, Laidlaw DH, Cabeen RP, et al. Brain structure and cognitive correlates of body mass index in healthy older adults. *Behav Brain Res*. 2015;278:342-347. doi:10.1016/j.bbr.2014.10.010.Brain.

161. Wickham H. Tidyverse: Easily install and load "Tidyverse" packages. 2017.

162. R Core Team. R: A language and environment for statistical computing. 2016. https://www.r-project.org/.

163. Blakemore S-J, Burnett S, Dahl RE. The role of puberty in the developing adolescent brain. *Hum Brain Mapp*. 2010;31(6):926-933. doi:10.1002/hbm.21052.

164. Tanaka-Arakawa MM, Matsui M, Tanaka C, et al. Developmental changes in the corpus callosum from infancy to early adulthood: A structural magnetic resonance imaging study. *PLoS One*. 2015;10(3):1-13. doi:10.1371/journal.pone.0118760.

165. Pujol J, Vendrell P, Junque C, Marti-Vilalta JL, Capdevila A. When does human brain development end? Evidence of corpus callosum growth up to adulthood. *Ann Neurol*. 1993;34(1):71-75.

166. Ladouceur CD, Peper JS, Crone E a., Dahl RE. White matter development in

adolescence: The influence of puberty and implications for affective disorders. *Dev Cogn Neurosci*. 2012;2(1):36-54. doi:10.1016/j.dcn.2011.06.002.

167. Lamantia A-S, Rakic P. Cytological and quantitative characteristics of four cerebral commissures in the rhesus monkey. *J Comp Neurol*. 1990;291:520-537.

168. Kullmann S, Callaghan MF, Heni M, et al. Specific white matter tissue microstructure changes associated with obesity. *Neuroimage*. 2016;125:36-44. doi:10.1016/j.neuroimage.2015.10.006.

169. Tamnes CK, Roalf DR, Goddings A, Lebel C. Diffusion MRI of white matter microstructure development in childhood and adolescence: Methods, challenges and progress. *bioRxiv Prepr*. 2017.

170. Paus T. How environment and genes shape the adolescent brain. *Horm Behav*. 2013. http://www.sciencedirect.com/science/article/pii/S0018506X13000925. Accessed April 6, 2014.

171. Mills KL, Lalonde F, Clasen LS, Giedd JN, Blakemore S-J. Developmental changes in the structure of the social brain in late childhood and adolescence. *Soc Cogn Affect Neurosci*. 2014;9(1):123-131. doi:10.1093/scan/nss113.

172. Loken E, Gelman A. Measurement error and the replication crisis. *Science.* 2017;355(6325):584-585.